

1 **BioRT-Flux-PIHM v1.0: a watershed biogeochemical reactive transport**  
2 **model**

3 Wei Zhi<sup>1</sup>, Yuning Shi<sup>2</sup>, Hang Wen<sup>1</sup>, Leila Saberi<sup>3</sup>, Gene-Hua Crystal Ng<sup>3</sup>, Kayalvizhi  
4 Sadayappan<sup>1</sup>, Devon Kerins<sup>1</sup>, Bryn Stewart<sup>1</sup>, Li Li<sup>1,\*</sup>

5 <sup>1</sup> Department of Civil and Environmental Engineering, The Pennsylvania State University, State  
6 College, PA 16802, USA

7 <sup>2</sup> Department of Ecosystem Science and Management, The Pennsylvania State University, State  
8 College, PA 16802, USA

9 <sup>3</sup> Department of Earth and Environmental Sciences, University of Minnesota, Twin Cities, MN  
10 55455, USA

11 \* Correspondence to [lili@engr.psu.edu](mailto:lili@engr.psu.edu)

12

## Abstract

13 Watersheds are the fundamental Earth surface functioning units that connect the land to  
14 aquatic systems. Many watershed-scale models represent hydrological processes but  
15 lack the representation of multi-component reactive transport processes. This has limited  
16 our capability to understand and predict solute export, water chemistry, and earth system  
17 response to changing climate and anthropogenic conditions. Here we present a recently  
18 developed BioRT-Flux-PIHM (BioRT hereafter) v1.0, a watershed-scale biogeochemical  
19 reactive transport model. The model augments the previously developed RT-Flux-PIHM  
20 that integrates land-surface interactions, surface hydrology, and abiotic geochemical  
21 reactions. It enables the simulation of 1) shallow and deep water partitioning to represent  
22 surface water, shallow soil water, and deeper groundwater; 2) biotic processes including  
23 plant uptake, soil respiration, and microbially mediated reactions such as nutrient  
24 transformation. The reactive transport part of the code has been verified against the  
25 widely used reactive transport code CrunchTope. BioRT-Flux-PIHM v1.0 has recently  
26 been applied in multiple watersheds under diverse climate, vegetation, and geological  
27 conditions. This paper briefly introduces the governing equations and model structure  
28 with a focus on new model developments. It also showcases one hydrology example that  
29 simulates shallow and deep water interactions, and two biogeochemical examples  
30 relevant to nitrate and dissolved organic carbon (DOC). These examples are illustrated  
31 in two simulation modes of varying complexity. One is the spatially lumped mode (i.e.,  
32 two land cells connected by one river segment) that focuses on processes and average  
33 behavior of a watershed. Another is the spatially distributed mode (i.e., hundreds of cells)  
34 that includes details of topography, land cover, and soil properties. Whereas the spatially  
35 lumped mode represents more of averaged properties and processes and temporal  
36 variations, the spatially distributed mode can be used to understand the impacts of spatial  
37 structure and identify hot spots of biogeochemical reactions.

## 38 1. Introduction

39 Watersheds are the fundamental Earth surface units that receive and process  
40 water, mass, and energy (Li, 2019;Li et al., 2020;Hubbard et al., 2018). Watershed  
41 processes include land surface interactions that regulate evapotranspiration and  
42 discharge, and water partitioning between shallow soil lateral flow going into streams  
43 versus downward flow and recharge into the deeper subsurface (Figure 1). Complex  
44 biogeochemical interactions occur among soil, water, roots, and microbes along water's  
45 flow paths, regulating gas effluxes (e.g., CO<sub>2</sub>) and solute export (Fatichi et al., 2019;van  
46 der Velde et al., 2010;Grathwohl et al., 2013).

47 These hydrological and biogeochemical processes determine how Earth surface  
48 systems respond to hydroclimatic forcing and human perturbations (van der Velde et al.,  
49 2014;Miller et al., 2020;Han et al., 2019). Understanding these processes remains  
50 challenging due to the complex process interactions. An example is the concentration-  
51 discharge (C-Q) relationships of solutes at stream and river outlets. Similar C-Q  
52 relationships have been observed for some solutes across watersheds under diverse  
53 geological and climatic conditions (Godsey et al., 2009;Basu et al., 2010;Moatar et al.,  
54 2017;Zarnetske et al., 2018;Godsey et al., 2019), whereas different solutes have shown  
55 contrasting patterns in the same watershed (Miller et al., 2017;Herndon et al.,  
56 2015;Musolff et al., 2015). A general theory that can explain contrasting C-Q observations  
57 (e.g., flushing vs. dilution behaviors) under diverse watershed characteristics and external  
58 conditions remains elusive. The lack of mechanistic understanding presents major  
59 roadblocks to forecasting water quality and earth system dynamics in the future.

60 One of the outstanding challenges is the lack of modeling tools that mechanistically  
61 link hydrological and biogeochemical processes at the watershed scale. Model  
62 development has advanced mostly within the disciplinary boundaries of hydrology and  
63 biogeochemistry (Li, 2019). Watershed hydrologic models focus on solving for water  
64 storage and fluxes (Fatichi et al., 2016). Reactive transport models (RTMs) have  
65 traditionally focused on transport and multi-component biogeochemical reactions mostly  
66 in groundwater systems with limited interactions with climate and other surficial conditions  
67 (Steeffel et al., 2015;Li et al., 2017b). Some integration crossing disciplinary boundaries

68 did occur in recent years. For example, SWAT (Soil & Water Assessment Tool) has a  
69 version that couples with the groundwater model MODFLOW and the surface water and  
70 groundwater quality model in RT3D (Bailey et al., 2017; Ochoa et al., 2020). CATHY  
71 (Catchment Hydrology) includes processes of pesticide decay (Gatel et al.,  
72 2019; Scudeler et al., 2016). Hydrologiska Byråns Vattenbalansavdelning (HBV) and the  
73 Hydrological Predictions for the Environment (HYPE) have modules that simulate  
74 processes relevant to nutrients and contaminants (Lindström et al., 2005; Lindström et al.,  
75 2010). While these models can simulate processes such as leaching of nutrients from  
76 agriculture lands (Lindström et al., 2005; Lindström et al., 2010; Bailey et al., 2017), they  
77 do not explicitly solve the multi-component reactive transport equations. In other words,  
78 reactions are often represented rudimentarily without honoring kinetics and  
79 thermodynamics theories in soil biogeochemistry and geochemistry. For example,  
80 nutrient leaching is calculated based on empirical equations without explicitly solving  
81 reactive transport equations. Reaction rates are represented using first-order decay  
82 (Gatel et al., 2019), assuming constant reaction rates that do not change with  
83 environmental conditions. Biogeochemical processes however are highly variable with  
84 seasonal dynamics and depend on local environments such as substrate availability, soil  
85 temperature, and soil moisture (Li et al., 2017a; HARTLEY et al., 2007). These models  
86 therefore cannot capture the temporal variations in environmental factors that regulate  
87 soil biogeochemical reactions and stream and water chemistry.

88 To fill this model capability need, we augmented the watershed model RT-Flux-  
89 PIHM (Bao et al., 2017) into BioRT-Flux-PIHM (BioRT hereafter). Compared to RT-Flux-  
90 PIHM, BioRT has two additions. One is the capability of simulating biotic processes  
91 including plant uptake of nutrients, soil respiration, and other microbe-mediated redox  
92 reactions. Examples include soil respiration that produces CO<sub>2</sub> and dissolved organic  
93 carbon (DOC), and nutrient transformation reactions such as nitrification and  
94 denitrification. The other is the addition of an optional deeper layer below shallow soil to  
95 enable the simulation of interacting deep water and shallow soil water flow (Figure 1).  
96 Here the deep water is loosely defined as the water below the soil zone, typically in less  
97 weathered, fractured subsurface that harbors relatively old and slow-moving groundwater  
98 contributing to streams. It is a fundamental component of the hydrologic cycle and water

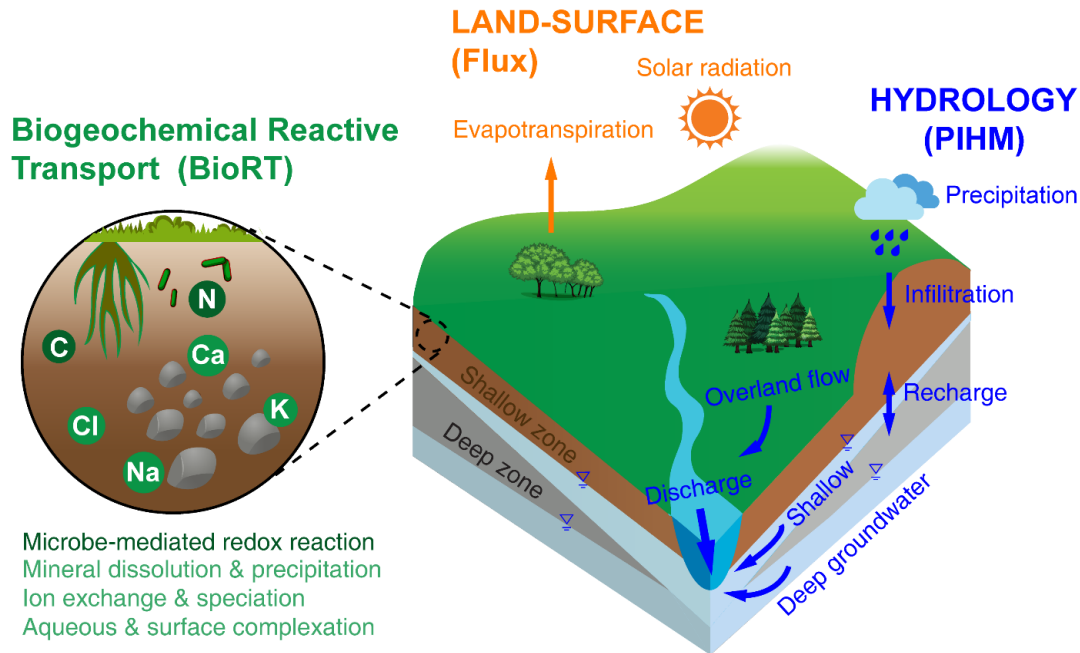
99 budget. The groundwater-surface water interactions also modulate land-atmospheric  
100 energy exchanges and soil moisture dynamics (Keune et al., 2016). Evidence has been  
101 mounting in recent years that deeper water below the shallow soil interacts with streams,  
102 introduces water with distinct chemistry, sustains base flow in dry times, and buffers  
103 climate variability (Gurdak, 2017;Green, 2016;Taylor et al., 2013). Stream chemistry often  
104 reflects distinct chemistry from shallow soil water and deeper groundwater at different  
105 time, i.e., the so called Shallow and Deep Hypothesis (Zhi et al., 2019;Zhi and Li,  
106 2020;Botter et al., 2020). Including the deep water component thus is essential for  
107 understanding mechanisms and predicting dynamics of water quality under changing  
108 climate and human conditions.

109 This paper introduces the new developments in BioRT. The paper starts with a  
110 brief overview of water and energy related processes. It then introduces governing  
111 equations and reaction kinetics used in BioRT, followed by three examples that illustrate  
112 the new capabilities. The examples include the surface water and groundwater  
113 interactions, nitrate transformation and transport, and the production and export of DOC.  
114 The model can be set up in both spatially lumped or spatially explicit modes. The source  
115 code and the examples shown here are archived on the Zenodo website  
116 (<https://doi.org/10.5281/zenodo.3936073>) and the GitHub website ([https://github.com/Li-  
117 Reactive-Water-Group/BioRT-Flux-PIHM](https://github.com/Li-Reactive-Water-Group/BioRT-Flux-PIHM)).

118

## 119 **2. Model overview**

120 BioRT-Flux-PIHM integrates three modules (Figure 1). The Flux module is for land-  
121 surface processes including surface energy balance, solar radiation, and ET (Shi et al.,  
122 2013). The hydrology module PIHM simulates water processes including precipitation,  
123 interception, infiltration, recharge, surface runoff, subsurface lateral flow, and deep water  
124 flow (Qu and Duffy, 2007). The BioRT module simulates solute transport reactions. The  
125 abiotic reactions included in RT-Flux-PIHM (Bao et al., 2017) are mineral dissolution and  
126 precipitation, aqueous and surface complexation, and ion exchange reactions. The newly  
127 added reactions include plant uptake of nutrients, soil respiration, microbe-mediated  
128 redox reactions (e.g., carbon decomposition and nutrient transformation).



129

130 **Figure 1.** A conceptual diagram for processes at the watershed scale. Land surface interactions  
 131 include processes such as energy balance, solar radiation, and evapotranspiration; hydrological  
 132 processes partition water between surface runoff, shallow soil water, and deeper water entering  
 133 the stream. Soil biogeochemical reactions include abiotic reactions such as weathering (e.g.,  
 134 mineral dissolution and precipitation), ion exchange, surface complexations), and biotic  
 135 processes such as plant uptake of nutrients, soil respiration, and other microbe-mediated  
 136 reactions. These processes are represented in three modules: The Flux module for land-surface  
 137 interactions, the PIHM module for catchment hydrology, and the BioRT module for  
 138 biogeochemical reactions. Conceptually the shallow zone is the shallow soil and weathered zone  
 139 that are more conducive to water flow (e.g., soil lateral flow or interflow). The deep zone refers  
 140 to the less weathered zone that often harbors the old and slow flowing groundwater. Reactions  
 141 can occur in both shallow and deep zones.

142

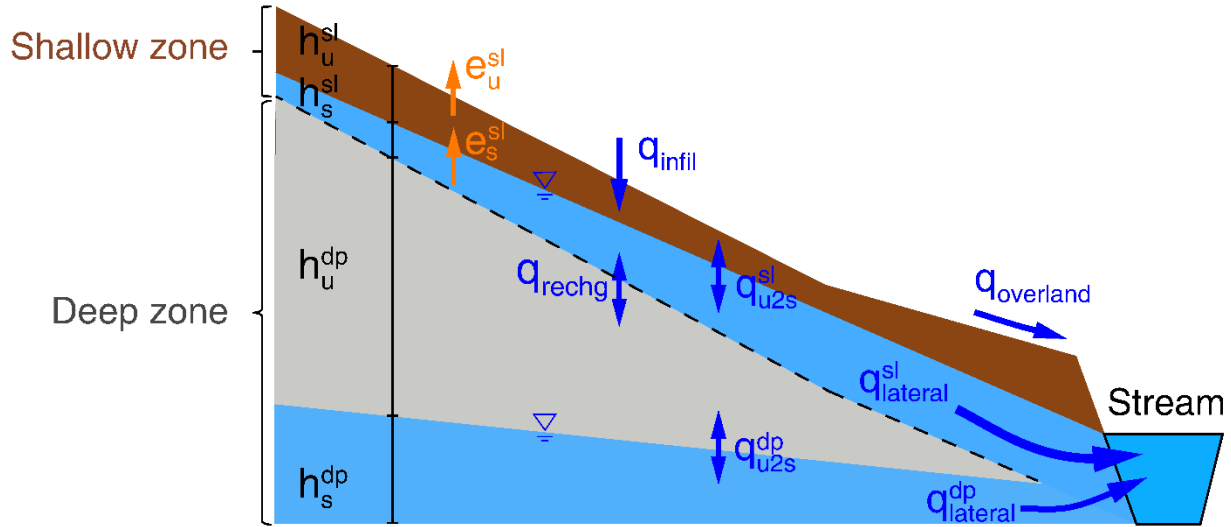
143 The land surface and hydrology modules solve for soil temperature and water  
 144 storage, from which water fluxes are calculated for surface runoff, shallow and deep water  
 145 fluxes. The BioRT module uses the calculated soil temperature, water storage, and water  
 146 fluxes to simulate solute transport (advective and diffusive/dispersive) and  
 147 biogeochemical reactions in both shallow and deep zones (see governing equations in  
 148 later sections). The reactions include kinetically controlled (e.g., microbe-mediated redox  
 149 reaction, mineral dissolution and precipitation) or equilibrium-controlled (e.g., ion  
 150 exchange, surface complexation (sorption), and aqueous complexation). Users can

151 define the types of reactions to be included and the form of reaction kinetics in input files.  
152 The output of BioRT includes the spatial distribution and time series of aqueous and solid  
153 concentrations, from which we can infer reaction rates.

154 The model can be set up running in either spatially lumped or spatially explicit  
155 modes. When running in spatially explicit mode, the simulation domain can be structured  
156 as prismatic grids based on topography. Each grid is partitioned into surface and shallow  
157 and deep subsurface layers. The surface layer calculates water flow above ground  
158 (surface runoff). The shallow zone is loosely defined as the highly permeable subsurface  
159 that contrasts the deep zone that is broadly defined as the lower permeability zone  
160 beyond the shallow zone. In many places, the shallow zone is the soil zone that is most  
161 conductive to water flow (e.g., lateral flow) and is responsive to hydroclimatic forcing. The  
162 deep subsurface zone is the less weathered layer that harbors the old ground water that  
163 contributes to stream flow. Note that these definitions differ from those in the hydrology  
164 community, which often refers to the shallow soil lateral flow as groundwater, in a way  
165 that distinguishes it from the surface runoff (Dingman, 2015). These source waters from  
166 different depths of the subsurface often have distinct solid and water chemistry, and are  
167 dominant at different hydrological conditions in different time of the year, as have been  
168 observed in many catchments and watersheds (Brantley et al., 2018;Zhi et al., 2019;Zhi  
169 and Li, 2020;Sullivan et al., 2016). The model is flexible for taking inputs from online data  
170 portals or local measurements and it can accommodate low data availability (see the  
171 following section of 5 for data need and domain setup).

172

### 173 **3. Governing equations and processes**



174  
 175 **Figure 2.** Hillslope view of the shallow and deep zones and relevant water flows. Streams  
 176 received water primarily from three water flows: the surface runoff ( $q_{\text{overland}}$ ), and lateral flow from  
 177 shallow zone ( $q_{\text{lateral}}^{\text{sl}}$ ), and the lateral flow that has been recharged and eventually come out from  
 178 deeper zone ( $q_{\text{lateral}}^{\text{dp}}$ ). The symbol of “h”, “e”, and “q” denotes water storage, evapotranspiration,  
 179 and water flow, respectively. The superscript letter “sl” and “dp” refer to shallow and deep zone,  
 180 respectively. The subscript letters “u” and “s” refer to unsaturated and saturated layers,  
 181 respectively. Detailed equations are in section 3.1 – 3.2. The terms “infil”, “u2s”, and “recharge”  
 182 refer to infiltration, unsaturated to saturated zones, and recharge.

183

### 184 3.1 Water equations

185 Flux-PIHM simulates surface runoff and a lumped subsurface flux into streams  
 186 without distinguishing shallow soil water and deeper groundwater flow paths. Mounting  
 187 evidence has shown that the shallow soil water and deeper groundwater have distinct  
 188 chemistry and are dominant at different times of the year (Xiao et al., 2021; Zhi and Li,  
 189 2020; Zhi et al., 2019). This means that a lumped subsurface flow cannot describe the  
 190 dynamics of stream chemistry. We therefore added deeper groundwater zone to simulate  
 191 deeper water flows that interact with streams. Each prismatic element now has three  
 192 zones in the vertical direction: surface (or above ground), shallow and deep zones in the  
 193 subsurface.

194 In each prismatic element  $i$ , the shallow zone includes unsaturated and saturated  
 195 water storages. The unsaturated zone receives water from the surface via infiltration and  
 196 flows vertically to the saturated zone. The saturated zone flows both vertically to the deep



197 zone (recharge) and laterally to neighboring grids  $j$  or the stream (lateral). The code  
 198 solves the following equations in the shallow zone:

$$199 \quad \theta_i^{sl} \frac{dh_{i,u}^{sl}}{dt} = q_{i,inf} - q_{i,u2s}^{sl} - e_{i,u}^{sl} \quad (1)$$

$$200 \quad \theta_i^{sl} \frac{dh_{i,s}^{sl}}{dt} = q_{i,u2s}^{sl} - q_{i,rechg} - e_{i,s}^{sl} + \sum_1^{N_{ij}} q_{ij}^{sl} \quad (2)$$

201 Where  $\theta_i^{sl}$  [ $\text{m}^3$  pore space/ $\text{m}^3$  total volume] is the shallow zone porosity in element  $i$ ;  $h_{i,u}^{sl}$   
 202 and  $h_{i,s}^{sl}$  [m] are the unsaturated and saturated water storage in the shallow zone,  
 203 respectively. The storages  $h$  here are the height of soil column with equivalent saturated  
 204 water, not the height of the pure water (100% volume) column. That is why porosity is in  
 205 the equation. For saturation zones, this height is needed to quantify the depths of water  
 206 tables and determines the direction of water flow between neighboring grids. The  
 207  $q_{i,inf}$  [m/s] is the infiltration rate from the surface to the shallow zone;  $q_{i,u2s}^{sl}$  [m/s] is the  
 208 vertical flow from the unsaturated layer to the saturated layer in the shallow zone;  $q_{i,rechg}$   
 209 [m/s] is the recharge rate from the shallow zone to the deep zone;  $e_{i,u}^{sl}$  and  $e_{i,s}^{sl}$  [m/s] are  
 210 evapotranspiration (ET) from the unsaturated and saturated layer in the shallow zone,  
 211 respectively;  $q_{ij}^{sl}$  [m/s] are the lateral flows in the shallow saturated layer between the  
 212 element  $i$  and its neighbor element  $j$ ;  $N_{ij}$  ( $\leq 3$ ) is the number of neighbor elements  $j$ . For  
 213 a prismatic element  $i$ , a boundary cell has one or two neighbors; a non-boundary cell has  
 214 three neighbors. ET is calculated by the Penman potential evaporation scheme (detailed  
 215 equations in Shi (2012)). A similar set of water equations for the deep zone are in the SI  
 216 (Eqn. S1 and S2).

217 Infiltration and vertical fluxes from the unsaturated to saturated layer in the shallow  
 218 zone are based on the Richards equation, in which hydraulic water head  $H$  (i.e., the  
 219 summation of water storage  $h$  and elevation head  $z$ ) and hydraulic conductivity  $K$   
 220 determine the fluxes:

$$221 \quad q_{i,inf} = K_{i,inf} \frac{H_{i,sur} - H_{i,u}^{sl}}{d_{i,inf}} \quad (3)$$

222 
$$q_{i,u2s}^{sl} = K_{i,V}^{sl} \frac{H_{i,u}^{sl} - H_{i,s}^{sl}}{0.5d_i^{sl}} \quad (4)$$

223 Where  $d_{i,inf}$  and  $d_i^{sl}$  [m] are the thickness of infiltration layer and shallow zone depth,  
 224 respectively;  $K_{i,inf}$  [m/s] is the hydraulic conductivity of the infiltration layer, the top 0.1 m  
 225 of the subsurface that has different conductivity from the rest of subsurface;  $K_{i,V}^{sl}$  [m/s] is  
 226 the hydraulic conductivity in the vertical direction (i.e., weighted average of macropore  
 227  $K_{i,macV}$  and soil matrix  $K_{i,satV}$ , Eqn. S7);  $H_{i,sur}$  [m] is the surface hydraulic water head (=  $h_{i,sur} + z_{i,sur}$ );  $H_{i,u}^{sl}$  and  $H_{i,s}^{sl}$  [m] are the shallow hydraulic water heads in the unsaturated  
 229 and saturated layer, respectively. The lateral flow in the shallow saturated layer is  
 230 calculated using Darcy's law:

231 
$$q_{ij}^{sl} = K_{ij}^{sl} \frac{H_{i,s}^{sl} - H_{j,s}^{sl}}{d_{ij}} \quad (5)$$

232 Where  $d_{ij}$  [m] is the distance between the centers of elements  $i$  and  $j$ ;  $K_{ij}^{sl}$  [m/s] is the  
 233 harmonic mean of shallow hydraulic conductivity in the horizontal direction between  
 234 elements  $i$  ( $K_{i,H}^{sl}$ ) and  $j$  ( $K_{j,H}^{sl}$ ). The interaction between the shallow saturated zone and  
 235 stream channel also follows Eqn. 5, except that the adjacent head is replaced by the level  
 236 of stream water. Similar to the shallow zone, hydrological equations in the deep zone are  
 237 detailed in the SI (Eqn. S1 – S8).

238

### 239 **3.2 Reactive transport equations**

240 The governing advection dispersion reaction (ADR) equation for an arbitrary solute  
 241  $m$  in an element  $i$  is as follows (Bao et al., 2017):

242 
$$V_i \frac{d(S_{w,i}\theta_i C_{m,i})}{dt} = \sum_1^{N_{ij}} \left( A_{ij} D_{ij} \frac{C_{m,j} - C_{m,i}}{d_{ij}} - q_{ij} A_{ij} C_{m,j} \right) + R_{m,i}, \quad m = 1, \dots, nm \quad (6)$$

243 Where  $V_i$  [m<sup>3</sup> total volume] is the total volume of element  $i$ ;  $S_{w,i}$  [m<sup>3</sup> water/m<sup>3</sup> pore space]  
 244 is soil water saturation;  $\theta_i$  [m<sup>3</sup> pore space/m<sup>3</sup> total volume] is the porosity;  $C_{m,i}$  [mol/m<sup>3</sup>  
 245 water] is the aqueous concentration of species  $m$ ;  $N_{ij}$  is the number of fluxes from

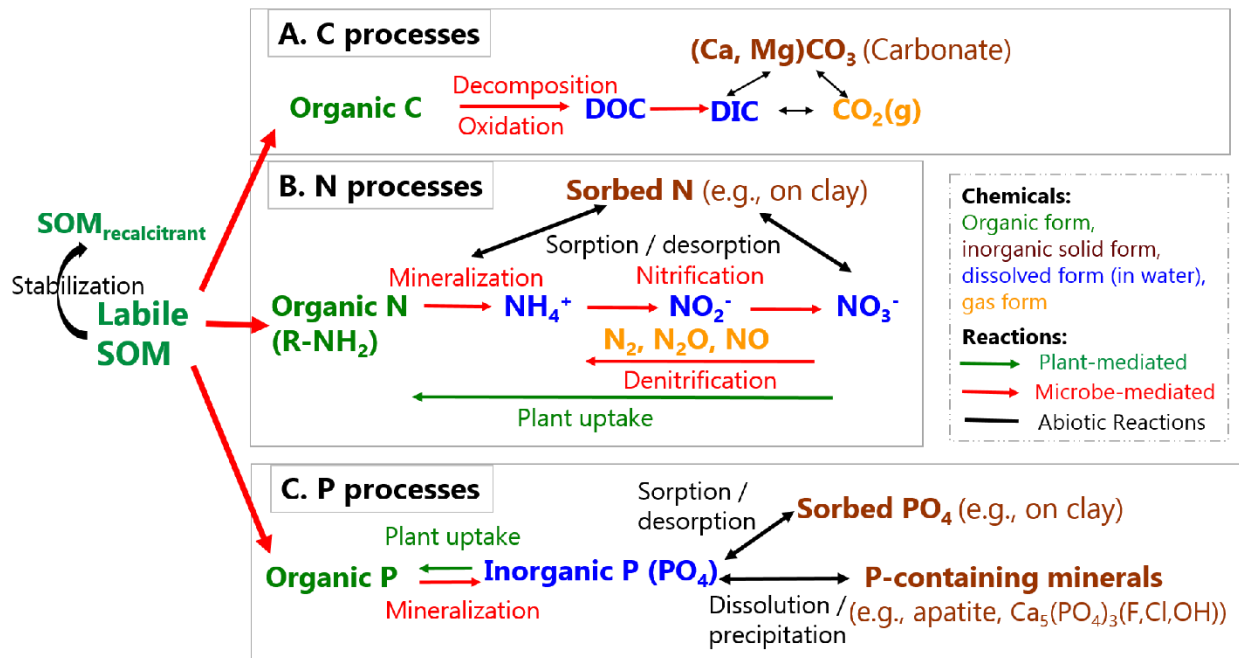
246 neighbor element  $j$  for element  $i$ ,  $N_{ij}$  is 2 for the unsaturated zone (infiltration, recharge)  
247 with only vertical flows and 5 for saturated zone with flux from (or to) the unsaturated  
248 zone, from (or to) the deeper zone, and fluxes between  $i$  and three neighbor elements  $j$   
249 in lateral flow directions for non-boundary grids;  $A_{ij}$  [ $\text{m}^2$ ] is the grid area shared by  $i$  and  
250 its neighbor grid  $j$ ;  $D_{ij}$  [ $\text{m}^2/\text{s}$ ] is the hydrodynamic dispersion coefficient (i.e., sum of  
251 mechanical dispersion and effective diffusion coefficient) normal to the shared surface  
252  $A_{ij}$ ;  $d_{ij}$  [ $\text{m}$ ] is the distance between the center of  $i$  and its neighbor elements  $j$ ;  $q_{ij}$  [ $\text{m}/\text{s}$ ]  
253 is the flow rate across  $A_{ij}$ ;  $R_{m,i}$  [ $\text{mol}/\text{s}$ ] is the total rate of kinetically controlled reactions in  
254 element  $i$  that involve species  $m$ ;  $nm$  is the total number of independent primary species  
255 to be solved for reactive transport equations. Equation (6) states that the change of solute  
256 mass (the left term) is driven by dispersive transport, advective transport, and reactions  
257 (i.e., the 1<sup>st</sup>, 2<sup>nd</sup>, and 3<sup>rd</sup> right-hand side terms, respectively).

258

### 259 **3.3 Biogeochemical processes and reaction kinetics**

#### 260 **3.3.1 Biogeochemical processes**

261 Here we discuss representative biogeochemical processes that involve plants and  
262 microbes that can be included in BioRT. BioRT differs from general water quality models  
263 that primarily target a few contaminants (e.g., N, P, metals). The framework of BioRT is  
264 flexible and the users can define reactions and solutes of interests in the input files. For  
265 abiotic reactions such as mineral dissolution and surface complexation or ion exchange,  
266 readers are referred to (Bao et al. (2017)). Generally speaking, shallow soils contain more  
267 weathered materials and soil organic matters (SOM) including roots, leaves, and  
268 microbes. SOM can be decomposed partially into organic molecules that dissolve in  
269 water, i.e., Dissolved Organic Carbon (DOC). It can also become oxidized completely  
270 into  $\text{CO}_2$ , which can emit back to the atmosphere in gas form (Davidson, 2006) or  
271 transport and enter streams in the form of dissolved inorganic carbon (DIC). With  
272 coexisting cations (e.g., Ca, Mg), DIC can precipitate out and become carbonate minerals  
273 (e.g.,  $\text{CaCO}_3$ ).



274  
 275 **Figure 3.** Biotic and abiotic reactions relevant to the transformation of soil organic matter (SOM).  
 276 SOM can become stabilized (recalcitrant) through sorption on clay and separation from reactants.  
 277 Labile OM can decompose into inorganic forms, releasing C, N, and P that further transform into  
 278 various forms (adopted from Li (2019), permission with Mineralogical Society of America).

279  
 280 OM decomposition releases organic nitrogen (R-NH<sub>2</sub>), which can further react to  
 281 become NH<sub>4</sub><sup>+</sup> and other nitrogen forms (N<sub>2</sub>, N<sub>2</sub>O, NO, NO<sub>2</sub><sup>-</sup>, NO<sub>2</sub>) (Figure 3). The gases  
 282 can emit back to the atmosphere. Denitrification requires anoxic conditions and occurs  
 283 less commonly in shallow soils owing to the pervasive presence of O<sub>2</sub> (Sebestyen et al.,  
 284 2019); denitrification can become important under wet conditions and in O<sub>2</sub>-depleted  
 285 groundwater aquifers. Phosphorous (P) can be in organic forms in organic matter, sorbed  
 286 on fine soil particles, dissolved in water, or in solid forms as P-containing minerals.  
 287 Transformation of nutrients occurs through various bio-mediated or abiotic reactions. A  
 288 representative P-containing mineral in the Earth's crust is apatite Ca<sub>5</sub>(PO<sub>4</sub>)<sub>3</sub>(F, Cl, OH).  
 289 Once liberated via rock dissolution, P is biologically assimilated and locked in organic  
 290 forms. These organic forms have very low solubility, allowing them to bind on and be  
 291 transported together with soil particles in the form of orthophosphate or pyro-diphosphate.

292  
 293 **3.3.2 Reaction kinetics in natural soils**

294 **Rate dependence on temperature and soil moisture.** Reactions such as soil  
 295 respiration and plant uptake typically depend on environmental conditions (temperature  
 296 or soil moisture). For example, in shallow oxic soils where organic carbon and O<sub>2</sub> are  
 297 often abundant, the rate law for carbon decomposition can be simplified to the following  
 298 form assuming microorganism concentrations are relatively constant.

$$299 \quad r = kAf(T)f(S_w)f(Z_w) \quad (7)$$

300 Where the reaction rate  $r$  [mol/s] depends on rate constant  $k$  [mol/m<sup>2</sup>/s], the surface area  
 301  $A$  [m<sup>2</sup>] is a lumped parameter that quantitatively represents SOM content and biomass  
 302 abundance,  $f(T)$  and  $f(S_w)$  describe the temperature and soil moisture dependence,  
 303 respectively,  $f(Z_w)$  can be included to account for the depth distribution of SOM (Seibert  
 304 et al., 2009), and  $Z_w$  [m] is the water table depth. An example for the depth distribution is  
 305  $f(Z_w) = \exp\left(-\frac{Z_w}{b_m}\right)$  (Weiler and McDonnell, 2006; Bai et al., 2016), with  $b_m$  as the depth  
 306 coefficient describing the gradient of SOM content over depth. Users can choose to  
 307 include either one or all of these dependencies in input or database files.

308 The temperature dependence follows a Q<sub>10</sub>-based form (Lloyd and Taylor,  
 309 1994; Friedlingstein et al., 2006; Hararuk et al., 2015) as follows:

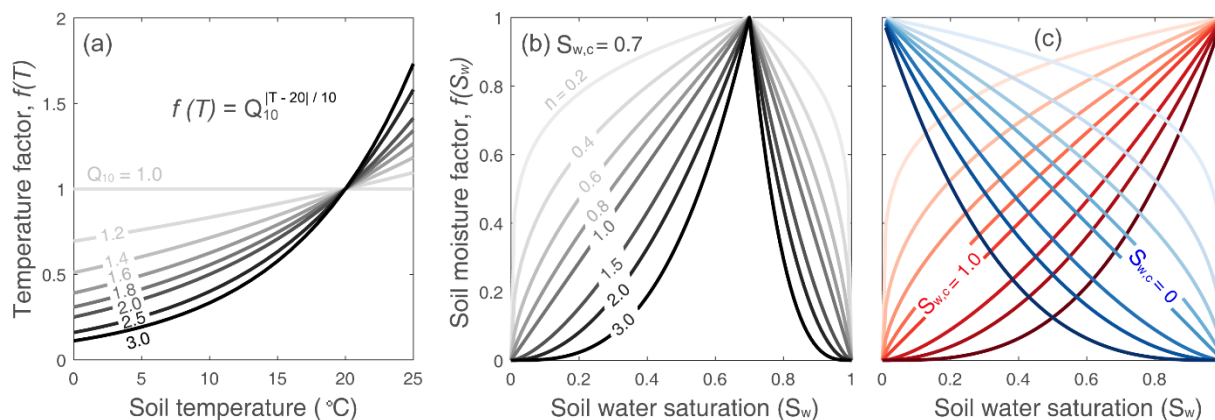
$$310 \quad f(T) = Q_{10}^{(T-20)/10} \quad (8),$$

311 where  $Q_{10}$  is the relative increase in reaction rates when temperature increases by 10 °C  
 312 (Davidson and Janssens, 2006). Values of  $Q_{10}$  (Figure 4a) can vary from 1.0 to 3.0,  
 313 depending on climatic conditions, substrate availability, and ecosystem type (e.g.,  
 314 grassland, forest) (Davidson et al., 2006; Liu et al., 2017). The mean values are in the  
 315 range of 1.4 to 2.5 (Zhou et al., 2009; Bracho et al., 2016). The  $Q_{10}$  value can be specified  
 316 in the input file.

317 The soil moisture dependence function  $f(S_w)$  is coded in the following form:

$$318 \quad \begin{cases} \left(\frac{S_w}{S_{w,c}}\right)^n, S_w \leq S_{w,c} \\ \left(\frac{1-S_w}{1-S_{w,c}}\right)^n, S_w > S_{w,c} \end{cases} \quad (9)$$

319 Here  $S_{w,c}$  [0 to 1] is the critical soil moisture at which rates are highest, and  $n$  is the  
 320 exponent reflecting the dependence of rates on soil moisture. A typical  $n$  value is 2 (Yan  
 321 et al., 2018) with a range between 1.2 and 3.0 (Hamamoto et al., 2010), depending on  
 322 soil structure and texture. As shown in Figure 4b, the form indicates an intermediate  
 323 critical soil moisture  $S_{w,c}$  at which  $f(S_w)$  reaches its maximum. When  $S_w \leq S_{w,c}$ ,  $f(S_w)$   
 324 increases with  $S_w$ ; when  $S_w > S_{w,c}$ ,  $f(S_w)$  decreases with  $S_w$  (Figure 4b) (Yan et al.,  
 325 2018). Under the extreme conditions of  $S_{w,c}$  equals to 0 or 1,  $f(S_w)$  monotonically  
 326 increase or decrease (Figure 4c). The two parameters,  $S_{w,c}$  and  $n$ , determines the shape  
 327 of the curve. They can be specified in input or database files. One can also choose not to  
 328 have temperature or soil moisture dependence by choosing parameters that would lead  
 329 to the value of exponent being zero.



330  
 331 **Figure 4.** Reaction rate dependence. (a) Function form of soil temperature dependence and (b,  
 332 c) soil moisture dependence for reaction rates. The  $f(T)$  takes  $Q_{10}$  form (Equation 8). The soil  
 333 moisture factor  $f(S_w)$  depends on  $S_{w,c}$  and  $n$  and soil water saturation  $S_w$  (Equation 9). The soil  
 334 moisture function can represent three types of behaviors: the threshold behavior (b,  $0 < S_{w,c} < 1$ ),  
 335 increase behavior (red in (c),  $S_{w,c} = 1$ ), and decrease behavior (blue in (c),  $S_{w,c} = 0$ ). Values of  $n$   
 336 = 1 leads to a linear threshold dependence of  $S_w$  while  $n < 1$  and  $n > 1$  lead to concave and  
 337 convex dependences, respectively.

338  
 339 **Rate dependence on substrates: Monod kinetics and biogeochemical redox**  
 340 **ladder.** Deeper groundwater aquifers often experience anoxic conditions that lead to  
 341 processes such as denitrification or methanogenesis. This can also happen in wetlands  
 342 or wet soils. Under such conditions, the rates of microbe-mediated redox reactions  
 343 depend not only on temperature and soil moisture as discussed above, they also depend

344 on concentrations of electron donors and non-oxygen electron acceptors (e.g., nitrate,  
345 iron oxides, sulfate) that are often limited under anoxic conditions (Bao et al., 2014;Li,  
346 2019;Benettin et al., 2020). The order of redox reactions typically follows the  
347 biogeochemical redox ladder, which is based on how much microbe can harvest energy  
348 by reducing different types of electron acceptors. Monod reaction rate laws are often used  
349 for quantifying rates of these redox conditions. These rate laws are detailed in the section  
350 S2 of Supporting Information. Users can combine these Monod rate laws and the  
351 temperature and soil moisture dependence described above, if needed.

352

### 353 **3.4 Plant related processes: root uptake of nitrate as an example**

354 Nutrient uptake by plants is complex and remains poorly understood. A variety of  
355 plant uptake models exists with varying degrees of complexity (Neitsch et al., 2011;Fisher  
356 et al., 2010;Cai et al., 2016). These models are mostly based on plant growth module or  
357 supply and demand approach that often requires detailed phenological and plant  
358 attributes including growth cycle, root age and biomass, nutrient availability, and carbon  
359 allocation, in addition to local temperature and soil moisture (Neitsch et al.,  
360 2011;Porporato et al., 2003;Dunbabin et al., 2002;Buysse et al., 1996;Fisher et al., 2010).  
361 Without detailed mechanistic understanding, we assume a simple and operational  
362 approach. In the Example 2 that we show later, for example, nitrate uptake was modelled  
363 with dependence on  $\text{NO}_3^-$  concentration, soil temperature and moisture, and rooting  
364 density (McMurtrie et al., 2012;Yan et al., 2012;Buljovic and Engels, 2001).

$$365 \quad r_{\text{uptake}} = k_{\text{uptake}} C_{\text{NO}_3^-} f(T) f(S_w) f_{\text{root}}(d_w) \quad (13)$$

$$366 \quad f_{\text{root}}(d_w) = \exp((-d_w + \delta) / \lambda) \quad (14)$$

367 Where  $k_{\text{uptake}}$  [L/s] is the nitrate uptake rate,  $f_{\text{root}}(d_w)$  is the normalized rooting density  
368 term in the range of 0 to 1 as a function of water depth to the groundwater ( $d_w$ ). The  
369 rooting term (Eqn. 14) was exponentially fitted ( $\delta = 0.013, \lambda = 0.20$ ) based on field  
370 measurements of root distribution along depth (Hasenmueller et al., 2017). It is common  
371 to observe root density decrease exponentially in forests (López et al., 2001). Other form  
372 of user-tailored plant uptake rate law can be added if needed.

373

#### 374 **4. Numerical scheme and model verification**

375 The system of differential equations for water storages (e.g., Eqn. 1 and 2, and Eqn.  
376 S1 and S2) are assembled into a global system of ordinary differential equations (ODEs).  
377 It is solved in CVODE (short for C-language Variable-coefficients ODE solver,  
378 <https://computing.llnl.gov/projects/sundials/cvode>), a numerical ODE solver in the SUIte  
379 of Nonlinear and Differential / ALgebraic equation Solvers (SUNDIALS) (Hindmarsh et  
380 al., 2005). In BioRT, the transport step is first solved with water by the preconditioned  
381 Krylov (iterative) method and the Generalized Minimal Residual Method (Saad and  
382 Schultz, 1986). All primary species in element I are then assembled in a local matrix  
383 and solved iteratively using the Crank-Nicolson and Newton-Raphson methods in  
384 CVODE (Bao et al., 2017).

385 **Model verification.** The BioRT module had been verified against CrunchTope  
386 under different transport and reaction conditions (Figures S1 – S7 in SI). CrunchTope is  
387 a widely used subsurface reactive transport model (Steefel and Lasaga, 1994; Steefel et  
388 al., 2015), and is often used as a benchmark to verify other reactive transport models.  
389 Verification was performed under simplified hydrological conditions with 1-D column and  
390 constant flow rates such that it focuses on advection, diffusion, dispersion, and  
391 biogeochemical reactions. Specifically, three cases were verified. The phosphorus case  
392 that involves kinetics-controlled apatite dissolution and thermodynamics-controlled  
393 phosphorous speciation was first tested for solution accuracy of the bulk code that was  
394 inherited from the original RT-Flux-PIHM. Soil carbon and nitrogen processes were  
395 further verified for solution accuracy of the augmented BioRT module. Table S7 shows  
396 an average percent bias and Nash Sutcliffe efficiency (NSE) of 1.1% and 0.98, indicating  
397 a robust performance for a variety of solutes under different transport and reaction  
398 conditions. Note NSE ranges from  $-\infty$  to 1, with NSE = 1 being the perfect fit (Moriassi et  
399 al., 2007).

400

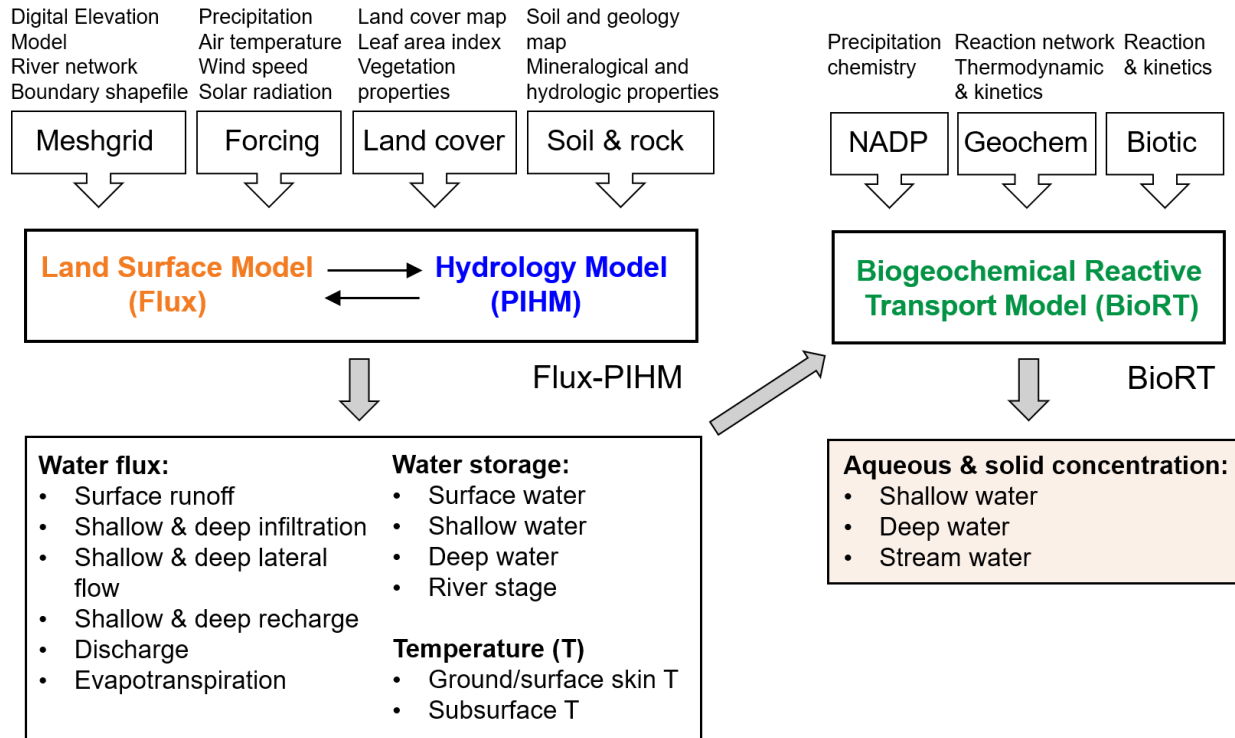
#### 401 **5. Model structure, data needs, and domain setup**

402 **Model structure.** The model takes meteorological forcing time series as input and  
403 solves for water storages and soil temperature, along with other hydrologic and land



404 surface states and fluxes (Figure 5). BioRT reads in the model output of water and  
405 temperature from Flux-PIHM, and solves the biogeochemical reactive transport  
406 equations. At the time scale of months to years that are typical for BioRT simulations,  
407 alterations in solid phase properties, including, porosity, permeability, and reactive  
408 surface area, are considered negligible such that hydrological parameters remain  
409 constant with time.

410 **Data needs.** The code sets up the model domain based on watershed  
411 characteristics including topography, land cover, and shallow and deep zone properties  
412 (Figure 5). When the model is used in a spatially distributed form, the model domain is  
413 set up using elevation, land cover, soil and geology maps supplied by the user. A useful  
414 data portal is the Geospatial Data Gateway (<https://datagateway.nrcs.usda.gov>). Another  
415 geospatial data source is the HydroTerre (<http://www.hydroterre.psu.edu/>), where users  
416 can obtain data on elevation, land cover, geology, and soil (Leonard and Duffy, 2013).  
417 Meteorological forcing data can be downloaded from the North American Land Data  
418 Assimilation Systems Phase 2 (NLDAS-2, <https://ldas.gsfc.nasa.gov/nldas/v2/forcing>).  
419 The vegetation forcing, i.e., Leaf Area Index (LAI), can be obtained from MODIS  
420 (Moderate Resolution Imaging Spectroradiometer, <https://modis.gsfc.nasa.gov/data>).  
421 Other vegetation properties (e.g., shading fraction, rooting depth) can be adopted from,  
422 for example, the Noah vegetation parameter table embedded in the Weather Research  
423 and Forecasting model (WRF; Skamarock and Klemp (2019)). Local measurements from  
424 meteorological stations and field campaigns (e.g., land cover, soil, geology) can be used  
425 in the model. Initial water and solid phase chemistry can be based on measurements or  
426 general knowledge of the simulated sites. The form of reaction rate laws can be defined  
427 in the input files and calibrated to reproduce field data. Reaction thermodynamics, mostly  
428 equilibrium constants, are from the geochemical database EQ3/6 by default (Wolery,  
429 1992). These reaction parameters can be modified when necessary. The model outputs  
430 include aqueous and solid concentrations of shallow and deep zone and stream water.



431  
 432 **Figure 5.** Model structure, input, and output of BioRT-Flux-PIHM. The Flux-PIHM takes in  
 433 watershed characteristics including topography (digital elevation model, DEM), land cover,  
 434 shallow and deep zone properties, and meteorological forcing time series and solves for water  
 435 storage, and ground and soil temperature. BioRT takes in water- and temperature-related output  
 436 from Flux-PIHM and additional inputs such as precipitation chemistry and shallow and deep water  
 437 chemistry and biogeochemical kinetics parameters, and solve for aqueous and solid  
 438 concentrations in the shallow and deep zone, and stream water. NADP stands for the National  
 439 Atmospheric Deposition Program.

440

441 **Domain set up: from simple, spatially lumped to complex, spatially distributed**

442 **domains.** The domain can be set up at different spatial resolutions with different numbers  
 443 of grids. A simple domain can be set up with two land grids representing two sides of a  
 444 watershed connected by one river cell. This setup uses averaged properties without  
 445 needs for larger spatial data. Alternatively, a complex domain can be set up to track “hot  
 446 spots” of biogeochemical reactions using many grids with explicit representation of spatial  
 447 details (e.g., topographic map, river network, land use map, soil and geology map, mineral  
 448 distribution). The model domain can be set up using PIHM-GIS  
 449 ([http://www.pihm.psu.edu/pihmgis\\_home.html](http://www.pihm.psu.edu/pihmgis_home.html)), a standalone GIS interface for watershed  
 450 delineation, domain decomposition, and parameter assignment (Bhatt et al., 2014). The

451 same processes (e.g., hydrology, reaction network) can be setup in both types of spatial  
 452 configurations. Auto-calibration is not built into the model, but a global calibration  
 453 coefficient approach is used to reduce parameter dimension and facilitate manual  
 454 calibration. A typical model application requires 20 to 30 hydrological parameters to be  
 455 calibrated. These parameters include land surface parameters (e.g., canopy resistance,  
 456 surface albedo), soil and geology parameters (e.g., hydraulic conductivity, porosity, Van  
 457 Genuchten, macropore properties) (Shi et al., 2013). Reaction-related parameters (e.g.,  
 458 reaction rate constant, mineral surface area,  $Q_{10}$ ,  $S_{w,c}$ , and  $n$ ) are additionally needed for  
 459 calibration, the number of which depends on the numbers of reactions involved in a  
 460 particular system.

461

## 462 **6. Model applications**

463 The original RT-Flux-PIHM has been applied to understand processes related to  
 464 the geogenic solutes of Cl and Mg at the Shale Hills watershed and for Na in a watershed  
 465 on Volcán Chimborazo in the Ecuadorian Andes (Table 1). The new BioRT-Flux-PIHM  
 466 has been demonstrated for understanding the dynamics of DOC and nitrate at Shale Hills  
 467 and Coal Creek. This section will present one hydrology and two biogeochemical  
 468 examples in the Susquehanna Shale Hills Critical Zone Observatory (SSHCZO), a small  
 469 headwater watershed in central Pennsylvania, USA. The mean annual precipitation is  
 470 approximately 1,070 mm and the mean annual temperature is 10°C (Brantley et al.,  
 471 2018). Soil carbon storage and respiration and nitrogen budget and fluxes have been  
 472 studied in detail (Andrews et al., 2011; Hasenmueller et al., 2015; Weitzman and Kaye,  
 473 2018). Modeling work has been conducted to understand hydrological dynamics (Shi et  
 474 al., 2013; Xiao et al., 2019), transport of the non-reactive tracer Cl, and the weathering-  
 475 derived solute Mg (Bao et al., 2017; Li et al., 2017a).

476

**Table 1.** Example Model applications of BioRT-Flux-PIHM

Watershed (location)	Size (km <sup>2</sup> )	Model domain	Modeled solute	Reactions (rate laws: 1, TST; 2, Monod based; 3, plant uptake)	Reference
-------------------------	----------------------------	-----------------	-------------------	--	-----------

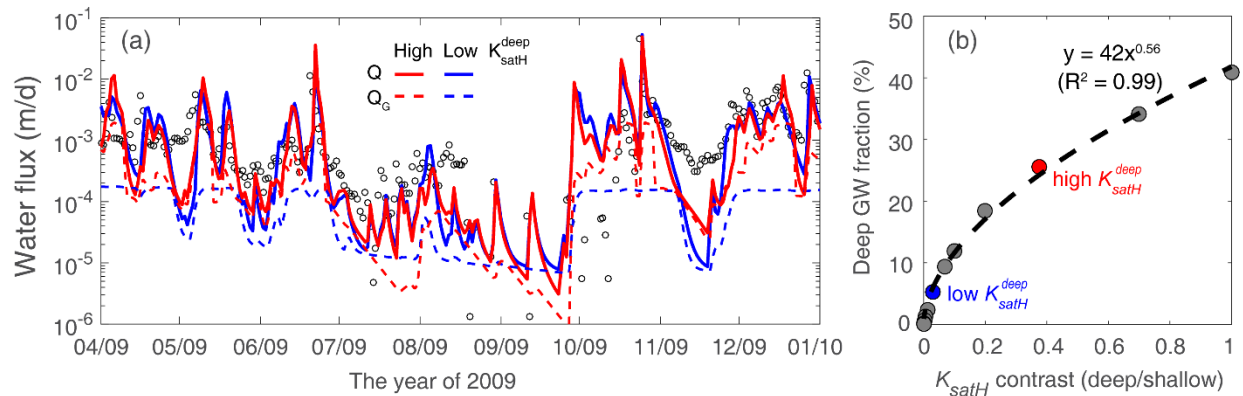
		Spatially distributed	Cl, Mg	<ul style="list-style-type: none"> <li>• Chlorite dissolution<sup>1</sup></li> <li>• Illite dissolution<sup>1</sup></li> <li>• Cation exchange</li> </ul>	Bao et al., 2017; Li et al., 2017
Shale Hills (PA, USA)	0.08	Spatially distributed	DOC	<ul style="list-style-type: none"> <li>• SOC decomposition<sup>2</sup></li> <li>• DOC sorption</li> </ul>	Wen et al., 2020
		Spatially lumped	NO <sub>3</sub> <sup>-</sup>	<ul style="list-style-type: none"> <li>• Soil N leaching<sup>2</sup></li> <li>• Denitrification<sup>2</sup></li> <li>• Plant uptake<sup>3</sup></li> </ul>	This work
Coal Creek (CO, USA)	53	Spatially lumped	DOC, Na	<ul style="list-style-type: none"> <li>• SOC decomposition<sup>2</sup></li> <li>• DOC sorption</li> <li>• Albite dissolution<sup>1</sup></li> </ul>	Zhi et al., 2019
Volcán Chimborazo (Ecuador)		Spatially distributed	Cl, Na, Ca, Mg, SiO <sub>2</sub>	<ul style="list-style-type: none"> <li>• Albite dissolution<sup>1</sup></li> <li>• Diopside dissolution<sup>1</sup></li> </ul>	Saberi et al. (2021)

477 Note: Transition State Theory (TST) is a classic kinetic rate law for mineral dissolution and  
478 precipitation (Brantley et al., 2008) (Eqn. S15); . SOC stands for soil organic carbon.

479

## 480 6.1 Example 1: Shallow and deep water interactions

481 The model was set up using the spatially lumped mode with two grids and one  
482 river grid characterized by average land cover, soil and rock properties based on previous  
483 work. The model assumed the dominant soil type (Weikert soil) at Shale Hills. The  
484 porosity of the deep zone was set to a tenth of the shallow soil porosity based on  
485 measurements of the groundwater aquifer (Brantley et al., 2018; Kuntz et al., 2011). In a  
486 headwater catchment like Shale Hills where the deep groundwater is most likely sourced  
487 from recharge, the deep groundwater contribution to the stream can be primarily  
488 controlled by the hydraulic conductivity ( $K_{satH}$ ) contrast between the deep and shallow  
489 zones (i.e.,  $K_{satH}^{dp} / K_{satH}^{sl}$ ). This is because the  $K_{satH}$  contrast determines the partitioning  
490 of infiltrating water between the shallow lateral flow and the downward recharge to the  
491 deep zone and then deep groundwater flow. Two cases of high (red) and low (blue)  $K_{satH}^{dp}$   
492 were set up to showcase the control of  $K_{satH}$  contrast on deep groundwater (Figure 6a).  
493 By changing the deep zone  $K_{satH}^{dp}$  from 2.6 to 0.22 (m/d), the annual deep groundwater  
494 ( $Q_G$ ) contribution to discharge ( $Q$ ) decreased from 26% to 5.2%, although the total stream  
495 discharge remains the same. This indicates that the changing  $K_{satH}^{dp}$  mostly changes the  
496 flow partitioning between the shallow soil flow and deeper groundwater flow into streams.



497

498 **Figure 6.** (a) Hydraulic conductivity ( $K_{satH}$ ) contrast controls the proportion of deep groundwater  
 499 ( $Q_G$ ). The cases of high ( $K_{satH}^{dp} = 2.6 \text{ m/d}$ , red) and low conductivity ( $K_{satH}^{dp} = 0.22 \text{ m/d}$ , blue) led  
 500 to 26% and 5.2% of annual  $Q_G$  contribution to discharge ( $Q$ ), respectively. (b) Deep groundwater  
 501 fraction as a function of  $K_{satH}$  contrast between the deep and shallow zone. The upper limit of the  
 502 deep / shallow  $K_{satH}$  contrast was set to 1 as most watersheds have smaller  $K_{satH}$  in the deep  
 503 zone than in the shallow zone. The two red and blue dots correspond to the two cases in left  
 504 panel.

505

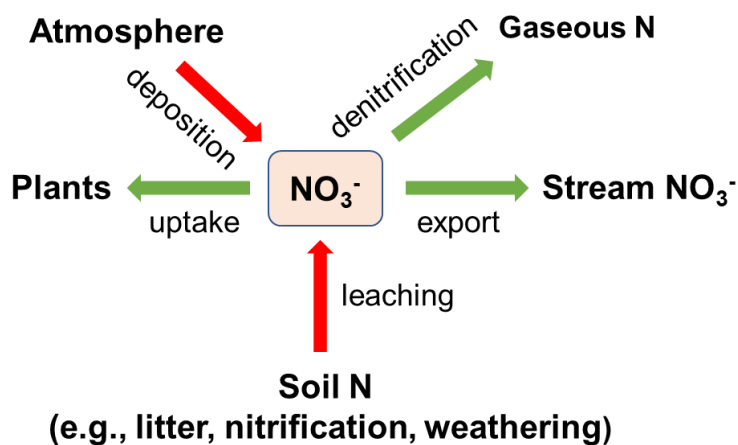
506 Several additional cases were further tested to examine the relationship between  
 507 deep groundwater fraction (%) of discharge and  $K_{satH}$  contrast. Figure 6b shows that the  
 508 deep groundwater fraction rapidly increases with the increasing ratio of  $K_{satH}^{dp} / K_{satH}^{sl}$ ,  
 509 reaching a limit when  $K_{satH}$  contrast is sufficiently high. The deep groundwater  
 510 contribution to the stream reaches  $\sim 40\%$  when  $K_{satH}^{dp}$  and  $K_{satH}^{sl}$  are equal. In natural  
 511 systems, we do see places, for example, karst formations, where groundwater contributes  
 512 to more than 40% (Hartmann et al., 2014; Husic, 2018). These places may have higher  
 513 deeper conductivity than shallow soils due to the development of highly conductive  
 514 conduits.

515

## 516 6.2 Example 2: Nitrate dynamics in a spatially implicit domain

517 This example focuses on nitrate ( $\text{NO}_3^-$ ), a dominant dissolved N form in water  
 518 (<https://criticalzone.org/shale-hills/data/datasets/>) (Weitzman and Kaye, 2018). The N  
 519 processes at Shale Hills include atmospheric N deposition, soil N leaching, stream export,  
 520 denitrification, and plant uptake (Figure 7). Based on field measurements, the  
 521 atmospheric deposition at the site is the dominant N input; N export via discharge is only

522 a small fraction (2.5%) of atmospheric N input. Most deposited N is tightly cycled by plants  
 523 or lost to the atmosphere via denitrification.



524  
 525 **Figure 7.** Modeled nitrogen processes in Example 2. Atmospheric N deposition is the major N  
 526 input; denitrification and plant uptake are the major N loss and sink. Export via discharge only  
 527 occupies a small fraction.

528  
 529 The soil N leaching process was represented using a lumped reaction that  
 530 generates  $\text{NO}_3^-$ . Conceptually this could represent the total rates of reactions including  
 531 the decomposition of soil organic matter (SOM), nitrification, and rock weathering that  
 532 generates  $\text{NO}_3^-$ . Its rate was assumed to depend on soil temperature and moisture and  
 533 follows the equation  $r_{leach} = kAf(T)f(S_w)$ , where  $r_{leach}$  [mol/s] is the leaching rate,  $k =$   
 534  $10^{-9.7}$  [mol/m<sup>2</sup>/s] is the leaching rate constant (Regnier and Steefel, 1999), and  $A$  [m<sup>2</sup>] is  
 535 the surface area that represents the contact area between substrates and N transforming  
 536 microbe, and  $f(T)$  and  $f(S_w)$  are soil temperature (Eqn. 8) and soil moisture (Eqn. 9)  
 537 functions, respectively. The surface area was calculated based on SOM volume fraction  
 538 [m<sup>3</sup>/m<sup>3</sup>], specific surface area (SSA, [m<sup>2</sup>/g]), substrate density [g/cm<sup>3</sup>], and element  
 539 volume [m<sup>3</sup>].

540 Denitrification converts  $\text{NO}_3^-$  to  $\text{N}_2$  gas under anaerobic conditions. Here this  
 541 process was modeled by the Monod rate law with DOC as the electron donor (Di Capua  
 542 et al., 2019),  $\text{NO}_3^-$  as the electron acceptor, and with an inhibition term  $f(O_2)$  (Eqn. S13).

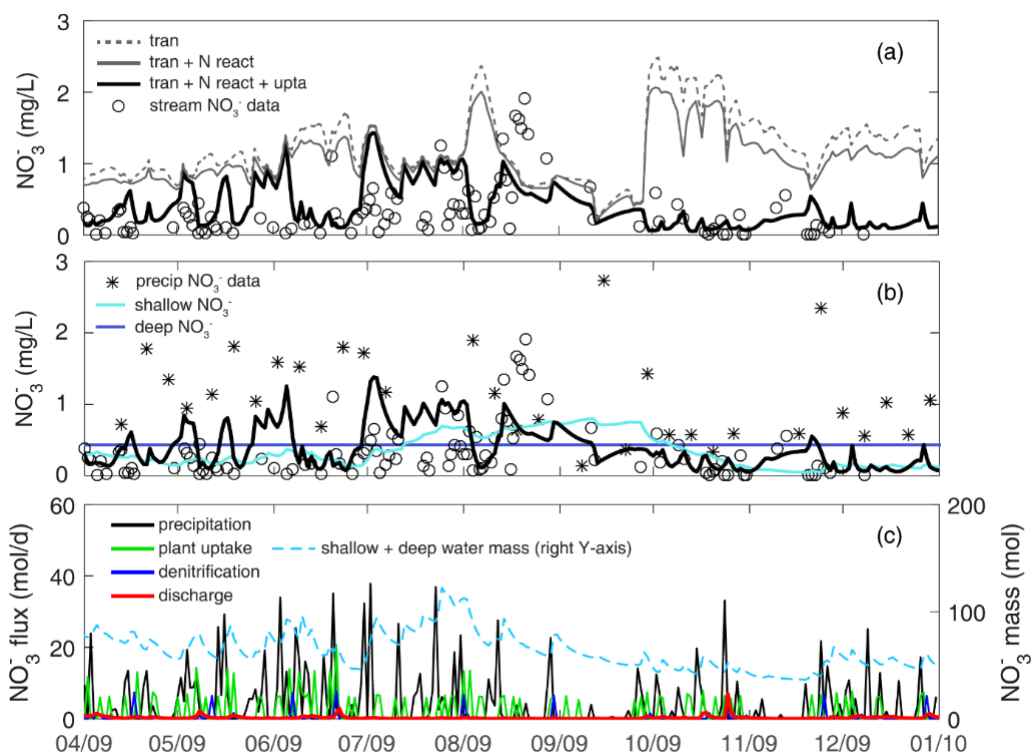
543 The reaction rate:  $r_{denitrification} = kA \frac{c_{DOC}}{K_{m,DOC} + c_{DOC}} \frac{c_{NO_3^-}}{K_{m,NO_3^-} + c_{NO_3^-}} f(O_2)f(T)f(S_w)$ , where  $k =$   
 544  $10^{-10}$  [mol/m<sup>2</sup>/s] is the denitrification rate constant (Regnier and Steefel, 1999), half-

545 saturation constants  $K_{m,DOC} = 15 [uM]$  and  $K_{m,NO_3^-} = 45 [uM]$  (Regnier and Steefel,  
546 1999). For soil N leaching and denitrification, the SSA were respectively tuned as  $1.6 \times$   
547  $10^{-6}$  and  $7.5 \times 10^{-5} [m^2/g]$  to reproduce observed stream nitrate dynamics. The calibrated  
548 values were orders of magnitude lower than the lab measured SSA of natural materials  
549 (e.g., SOM,  $0.6 \sim 2 m^2/g$ ) (Rutherford et al., 1992). Such discrepancies between  
550 calibrated effective reactive surface area (i.e., solid-water contact area) and lab measured  
551 absolute surface area are consistent with other observations in literature (Li et al.,  
552 2014; Heidari et al., 2017; Wen and Li, 2017, 2018). The uptake rate constant was  
553 calibrated by constraining the partitioning of N transformation flux between denitrification  
554 and plant uptake by the ratio of 1:5, a value estimated from field measurements of  
555 gaseous N outputs ( $3.53 \text{ kg-N/ha/yr}$ ) and plant N uptake ( $18.3 \text{ kg-N/ha/yr}$ ) (Weitzman and  
556 Kaye, 2018). The uptake rate constant in the deep zone ( $> 2 \text{ m}$  in depth) was considered  
557 negligible (Hasenmueller et al., 2017). Groundwater nitrate was initialized as  $0.43 \text{ mg/L}$ ,  
558 the average of measured groundwater concentration during 2009 - 2010.

559

560 **Temporal nitrate dynamics.** Three cases were set up to understand and quantify the  
561 effects of different processes in determining nitrate dynamics (Figure 8a). The *transport-*  
562 *only* case (dashed line, *tran*) simulates nitrate input from precipitation (at  $1.4 \pm 0.96 \text{ mg/L}$ ,  
563 based on the 2009 data of NADP PA42 site) and N transport but without any reactions. It  
564 overestimated stream nitrate data ( $0.33 \pm 0.39 \text{ mg/L}$ ) throughout the year. The *transport*  
565 *+ N reactions* case (gray line, *tran + N react*) has denitrification and soil N leaching  
566 processes but not plant uptake. These two reactions lowered the nitrate concentration  
567 slightly, as these two processes compensate each other in adding and removing nitrate  
568 from water. The *transport + N reactions + uptake* case (thick black line, *tran + N react +*  
569 *upta*) have all processes. It significantly lowered the nitrate concentration, especially in  
570 April-May and October-December. Nitrate peaks from May to July, exhibiting comparable  
571 levels of high nitrate concentration (Figure 8b). It is noticeable that the three cases almost  
572 overlapped at these overestimated short nitrate peaks, suggesting nitrate-rich  
573 precipitation may not be routed into the subsurface where denitrification and plant uptake  
574 could occur.

575 Although precipitation from April to August accounted for 70% of the total  
 576 simulation period, larger storm events in October contributed more to nitrate export.  
 577 Deeper groundwater had higher nitrate concentration than shallow water, because most  
 578 plant uptake occurred in the shallow zone. The nitrate fluxes into the deeper zone  
 579 however only contributed 26% of stream nitrate export at the annual scale, due to the  
 580 relatively small groundwater contribution (9.5%) to the stream. Denitrification and plant  
 581 uptake largely occurred during wet spring with leaves growing. Denitrification peaks often  
 582 appeared after major storm events because wet conditions facilitate denitrification.  
 583 Comparing the three outfluxes (Figure 8c), nitrate export via discharge (red) was  
 584 negligible compared to denitrification (blue) and plant uptake (green). At the annual scale,  
 585 stream export accounted for 9.5%, whereas denitrification and plant uptake took up 15%  
 586 and 75% of deposited  $\text{NO}_3^-$ , respectively. In other words, as Nitrate enters this system via  
 587 precipitation, plant uptake can play a significant role in reducing nitrate level, indicating  
 588 precipitated nitrate is tightly cycled in the system.



589  
 590 **Figure 8.** Stream nitrate dynamics and fluxes at Shale Hills in Example 2. (a) Three simulation  
 591 scenarios with different processes are demonstrated here: *transport-only* (dashed line, *tran*),  
 592 *transport + N reaction* (gray line, *tran + N react*), *transport + N reaction + plant uptake* (thick black

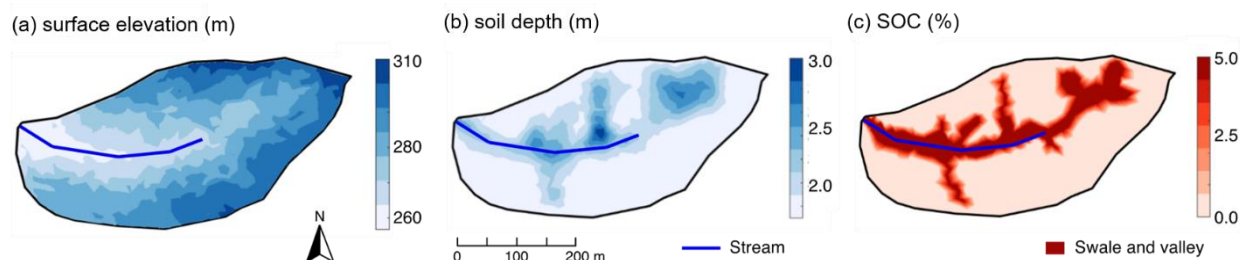


593 line,  $tran + N_{react} + u_{pta}$ ), where N reactions include both nitrate leaching and denitrification (see  
594 Figure 7); (b) nitrate concentration in precipitation, shallow and deep water; (c) nitrate fluxes and  
595 budget. Note that nitrate leaching was ignored in (b) due to its minimal flux as N deposition from  
596 rainfall was the dominant input (Weitzman and Kaye, 2018).

597

### 598 **6.3 Example 3: DOC production and export in a spatially distributed domain**

599 This example showcases the application of BioRT-Flux-PIHM in a spatially  
600 distributed mode. This work has been documented with full details in Wen et al. (2020).  
601 Here we only introduce some key features and capabilities in the spatially distributed  
602 mode. The Shale Hills catchment was discretized into 535 prismatic land elements and  
603 20 stream segments through PIHMgis based on the topography (Figure 9a). The  
604 heterogeneous distributions of soil depth and solid organic carbon within the domain  
605 (Figure 9b-c) were interpolated through ordinary kriging based on field surveys (Andrews  
606 et al., 2011;Lin, 2006). Other soil and mineralogy properties such as hydraulic  
607 conductivity, van Genuchten parameters, and ion exchange capacity were spatially  
608 distributed following intensive field measurements (Jin and Brantley, 2011;Jin et al., 2010)  
609 ([criticalzone.org/shale-hills/data/](https://criticalzone.org/shale-hills/data/)).



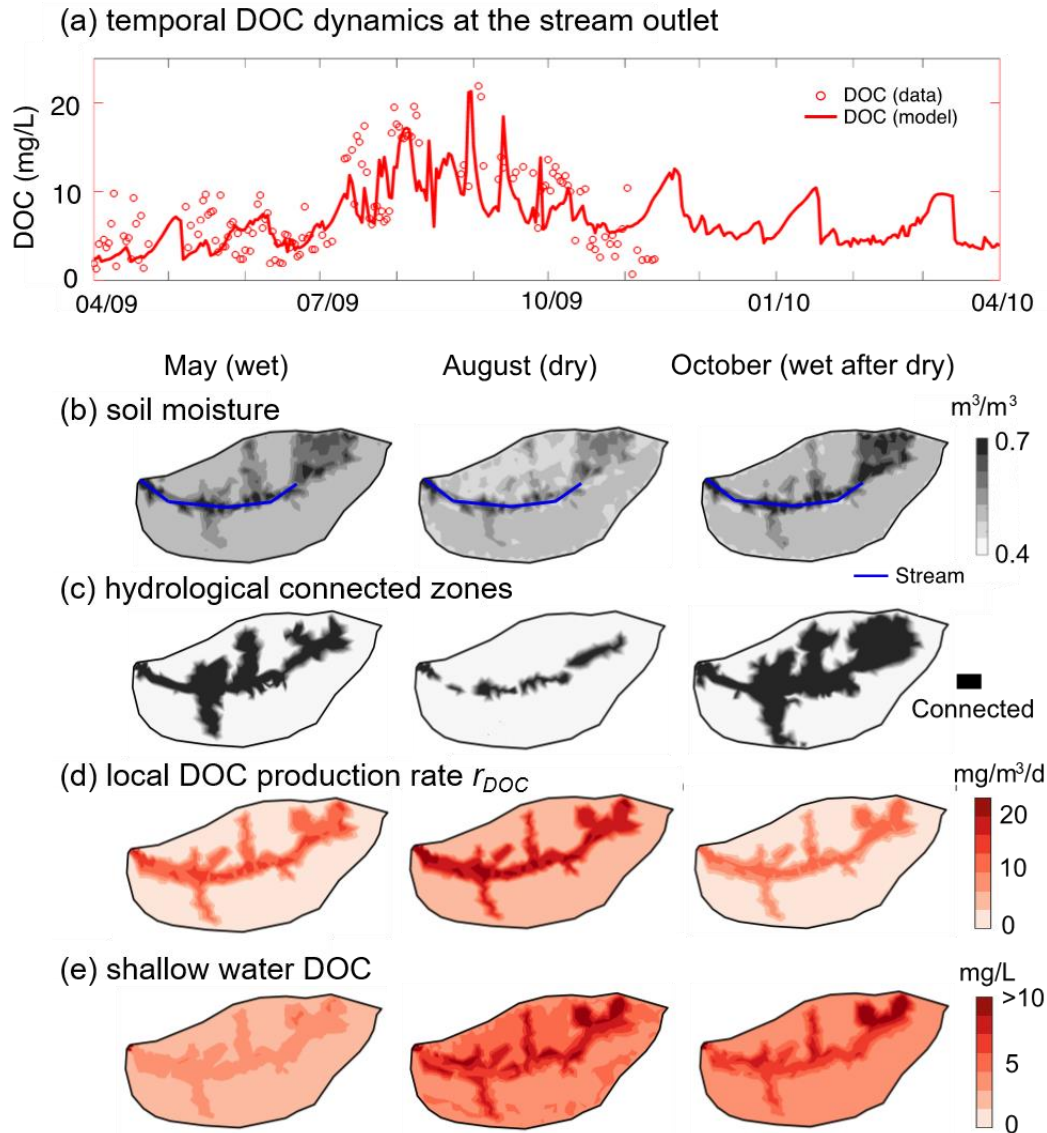
610  
611 **Figure 9.** Attributes of Shale Hills in the spatially distributed mode in Example 3: (a) surface  
612 elevation, (b) soil depth, and (c) soil organic carbon (SOC). The surface elevation was generated  
613 from lidar topographic data ([criticalzone.org/shale-hills/data/](https://criticalzone.org/shale-hills/data/)); Soil depths and SOC were  
614 interpolated using ordinary kriging based on field surveys (Andrews et al., 2011;Lin, 2006). The  
615 SOC distribution in (c) was further simplified using the high, uniform SOC (5% v/v) in swales and  
616 valley soils based on field survey (Andrews et al., 2011). Swales and valley floor areas were  
617 defined based on surface elevation via field survey and a 10 m resolution digital elevation model  
618 (Lin, 2006).

619  
620 **Temporal and spatial patterns of DOC production and export.** The model outputs  
621 followed the general trend of stream DOC measurements with the model evaluation index

622 NSE of 0.55 for monthly DOC concentration (Figure 10a). NSE values greater than 0.5  
623 are considered good performance for monthly water quality model (Moriassi et al., 2015).  
624 The model reproduced high DOC values (~15 mg/L) in the dry periods (July-September).  
625 The model enabled the identification of reaction hot spots. In May when soil water is  
626 relatively abundant, the valley and swales with deeper soils (Figure 10b) are generally  
627 wetter compared to the hillslope and ridgetop, and are hydrologically connected to the  
628 stream (Figure 10b, c). The distribution of local DOC production rate  $r_{DOC}$  and DOC  
629 concentration followed that of SOC (Figure 10c) and water content (Figure 10b). Low  $r_{DOC}$   
630 in relatively dry planar hillslopes and uplands resulted in low soil water DOC. The average  
631 stream DOC (~5 mg/L) reflected soil water DOC in the valley and swales.

632 In August, the hydrologically-connected zones with high water content shrank to  
633 the vicinity of the stream and river bed. With high temperature in summer,  $r_{DOC}$  increased  
634 by 2-fold from May across the whole catchment while still exhibited the highest values in  
635 the SOC-rich regions. Soil water DOC concentration increased by a factor of 2 because  
636 the produced DOC was trapped in low soil moisture areas that were not hydrologically  
637 connected to the stream. In the north side with low water content (Figure 10b), the soil  
638 water DOC (~7 mg/L in average) accumulated more than the south side (~5 mg/L in  
639 average). The high shallow water DOC (~10 mg/L) in the stream vicinity dominated the  
640 stream DOC in August.

641 In October, precipitation wetted the catchment again. The hydrologically  
642 connected zones expanded beyond swales and the valley to the upland hillslopes (Figure  
643 10c). The increase in hydrological connectivity zones favored the mixing of shallow water  
644 DOC sourced from upland hillslopes (low DOC), swales, and valley (high DOC) into  
645 stream rather than only from the stream vicinity with high DOC in the dry August, leading  
646 to a drop in stream DOC.



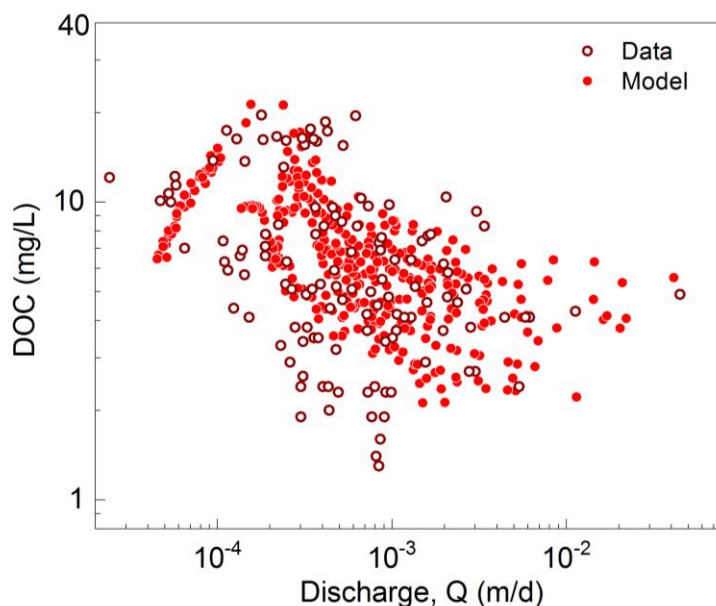
647

648 **Figure 10.** (a) Temporal dynamics of stream DOC concentration; spatial profiles of (b) shallow  
 649 soil moisture, (c) hydrologically connected zones, (d) local DOC production rates  $r_{DOC}$  and (e)  
 650 shallow water DOC concentration in May (wet), August (dry), and October (wet after dry) of 2009.  
 651 The soil DOC and  $r_{DOC}$  were high in swales and valley with relatively high shallow water and SOC  
 652 content. August had the highest shallow water DOC concentration compared to May and October,  
 653 because most DOC accumulated in zones that are disconnected to the stream.

654

655 **C-Q patterns.** The DOC C-Q relationship showed a non-typical pattern with flushing first  
 656 and transitioning into a dilution pattern, with an overall C-Q slope  $b = -0.23$  (Figure 11).  
 657 At low discharges ( $< 1.8 \times 10^{-4}$  m/d) in the summer dry period, the stream DOC mainly  
 658 came from the organic-rich swales and valley floor zones with high soil water DOC (Figure

659 10e). With discharge increasing in wetter period (i.e., spring and fall), the contribution  
660 from planar hillslopes and uplands with lower DOC concentration increased (Figure 10e),  
661 leading to the dilution of stream DOC.



662  
663 **Figure 11.** Relationships between daily discharge ( $Q$ ) and stream DOC concentration. With the  
664 increasing  $Q$ , the stream water first shifted from the dominance of groundwater with low DOC at  
665 very low discharge to the predominance of organic-rich soil water from swales and valley at  
666 intermediate discharge. As the discharge increases further, the stream water switches to the  
667 dominance of high flow with lower DOC water from planar hillslopes and uplands, resulting in a  
668 dilution C-Q pattern (modified from Wen et al., 2020).

669  
670 **7. Discussion**

671 BioRT-Flux-PIHM brings the reactive transport modeling capabilities to the  
672 watershed scale, enabling the simulation of subsurface shallow and deep flow paths and  
673 biogeochemical reactions influenced by hydroclimatic conditions and land-surface  
674 interactions. The expanded model capability of simulating bio-mediated processes such  
675 as plant uptake, soil respiration, and microbe-mediated redox reactions enables the  
676 simulation of carbon and nutrient cycling in the shallow subsurface. The inclusion of the  
677 deep groundwater zone allows the exploration of the effects of subsurface structure on  
678 hydrological partitioning between shallow soil lateral flow and deep groundwater, and their  
679 relationships with stream discharge. Although not shown here, the model can also  
680 simulate deeper groundwater coming from regional aquifers across the outer boundary.

681 This can be particularly useful for watersheds of higher stream orders, where a large  
682 proportion of deep water may come from nearby regional aquifers.

683 The advantage and disadvantages of simple versus complex models have long  
684 been debated in the modeling community (Fatichi et al., 2016;Li et al., 2020;Wen et al.,  
685 2021). The computational cost of solving a spatially distributed, nonlinear, multi-  
686 component reactive transport model is high, posing challenges for the application of  
687 ensemble-based analysis. With additional reactions and transport processes, the model  
688 includes more functions (such as reaction kinetic rate laws) and parameters (e.g., reaction  
689 rate constants, surface area) than hydrological models. The complexity brings in issues  
690 of equifinality, uncertainty, and data demands (Beven, 2001, 2006;Kirchner et al., 1996).  
691 These issues will persist even though reactive transport models will be constrained by  
692 additional chemical data.

693 It is in this spirit of balancing the cost and gain that we present both spatial  
694 distributed and lumped modes for the BioRT model (Li et al., 2020). Compared to the  
695 distributed version, the spatially implicit model requires less spatial data and is  
696 computationally inexpensive. It can assess the average dynamics of water and solute  
697 dynamics and focus on the interacting processes without resolving spatial details. The  
698 lumped approach can accommodate basins with low data availability, and it can be easier  
699 for students to learn. In contrast, spatially explicit representations enable the exploration  
700 of the “hot spots” (e.g., swales and riparian zones with high soil water DOC concentrations  
701 in Figure 10e) and their contribution to stream chemistry at different times. Spatial  
702 heterogeneities in watershed properties (e.g., soil types and depth, lithology, vegetation,  
703 biomass, and mineralogy) are ubiquitous in natural systems and are challenging to  
704 resolve. A general understanding of the linkage between local catchment features and  
705 catchment-scale dynamics (e.g., stream concentration dynamics and solute export  
706 pattern) is often lacking. The spatially distributed model provides a tool to explore these  
707 questions. Ultimately, the choice of the model complexity level depends on research  
708 questions that the model is set to answer and the available data. At the end, we all need  
709 to balance cost and gain when deciding to use a simple or complex model, striving to be  
710 “simple but not simplistic” (Beven and Lane, 2019).

## 711 **8. Summary and conclusion**

712 This paper introduces the watershed-scale biogeochemical reactive transport code  
713 BioRT (short for BioRT-Flux-PIHM). The code integrates processes of land-surface  
714 interactions, surface hydrology, and multi-component biogeochemical reactive transport.  
715 The new development enables the simulation of 1) biotic reactions including plant uptake,  
716 soil respiration, and microbe-mediated redox reactions, and 2) surface water interactions  
717 with groundwater from deeper subsurface that still interacts with streams. BioRT has been  
718 verified against the widely used reactive transport code CrunchTope for soil carbon,  
719 nitrogen, and phosphorus processes. It has been applied to understand carbon, nitrogen,  
720 and weathering processes at Shale Hills in Pennsylvania, Coal Creek in Colorado, and  
721 Volcán Chimborazo watershed in Andes in Ecuador. Here we showcase the modeling  
722 capability of surface-groundwater interactions and reactive transport processes relevant  
723 to nitrate and DOC in Shale Hills in two simulation modes. One is in a spatially lumped  
724 mode using averaged properties and another is in a spatially distributed mode with  
725 consideration of spatial heterogeneity. Results show that the deep groundwater flow that  
726 interacts with the stream is primarily controlled by the hydraulic conductivity contrast  
727 between shallow and deep zone. biogeochemical reactions in shallow soil primarily  
728 determine the stream water chemistry under high flow conditions. The spatially lumped  
729 method with two lumped grids can capture the temporal dynamics of average behavior  
730 and mass balance; the spatially distributed running mode can be used to understand the  
731 spatial dynamics and to identify “hot spots” of reactions. The code can be used for  
732 biogeochemical reactive transport simulations in watersheds under diverse climate, land  
733 cover, and geology conditions.

734

735 **Data availability.** Field data (e.g., discharge, stream chemistry) is archived at Shale Hills  
736 data portal: <http://criticalzone.org/shale-hills/data/datasets/> or maintained at HydroShare:  
737 <https://www.hydroshare.org/group/147>.

738

739 **Code availability.** The current model release (BioRT-Flux-PIHM v1.0) is archived at:  
740 <https://doi.org/10.5281/zenodo.3936073>. Documentation, source code, and examples  
741 are available at GitHub repository: [https://github.com/Li-Reactive-Water-Group/BioRT-](https://github.com/Li-Reactive-Water-Group/BioRT-Flux-PIHM)  
742 [Flux-PIHM](https://github.com/Li-Reactive-Water-Group/BioRT-Flux-PIHM).

743

744 **Competing interests.** The authors declare that they have no conflict of interest.

745

746 **Author contributions.** LL conceived the model idea and oversaw the model  
747 development. WZ coded the BioRT module, verified the code against the benchmark  
748 reactive transport model CrunchTope, and applied and tested the model at Shale Hills  
749 watershed. YS developed the deep groundwater component and integrated the BioRT-  
750 Flux-PIHM v1.0 into the MM-PIHM family. WH, LS, KS, DK, BS, and GHCN tested the  
751 code during its development and contributed study cases.

752

753 **Acknowledgement.** We acknowledge the funding support from the Department of  
754 Energy, Subsurface Biogeochemistry Program DE-SC0020146, National Science  
755 Foundation Hydrological Sciences EAR-1758795. LS and GCN were supported by  
756 National Science Foundation Grant EAR-1759071. We appreciate data from the  
757 Susquehanna Shale Hills Critical Zone Observatory (SSHCZO) supported by National  
758 Science Foundation Grant EAR – 0725019 (C. Duffy), EAR – 1239285 (S. Brantley), and  
759 EAR – 1331726 (S. Brantley). Data were collected in Penn State's Stone Valley Forest,  
760 which is funded by the Penn State College of Agriculture Sciences, Department of  
761 Ecosystem Science and Management, and managed by the staff of the Forestlands  
762 Management Office.

763 **References**

- 764 Andrews, D. M., Lin, H., Zhu, Q., Jin, L., and Brantley, S. L.: Hot spots and hot moments of dissolved organic  
765 carbon export and soil organic carbon storage in the Shale Hills catchment, *Vadose Zone Journal*, 10, 943-  
766 954, 2011.
- 767 Bai, J., Zhang, G., Zhao, Q., Lu, Q., Jia, J., Cui, B., and Liu, X.: Depth-distribution patterns and control of soil  
768 organic carbon in coastal salt marshes with different plant covers, *Sci Rep-Uk*, 6, 34835,  
769 10.1038/srep34835, 2016.
- 770 Bailey, R., Rathjens, H., Bieger, K., Chaubey, I., and Arnold, J.: SWATMOD-Prep: Graphical User Interface  
771 for Preparing Coupled SWAT-MODFLOW Simulations, *JAWRA Journal of the American Water Resources*  
772 *Association*, 53, 400-410, <https://doi.org/10.1111/1752-1688.12502>, 2017.
- 773 Bao, C., Wu, H., Li, L., Newcomer, D., Long, P. E., and Williams, K. H.: Uranium Bioreduction Rates across  
774 Scales: Biogeochemical Hot Moments and Hot Spots during a Biostimulation Experiment at Rifle, Colorado,  
775 *Environmental Science & Technology*, 48, 10116-10127, 10.1021/es501060d, 2014.
- 776 Bao, C., Li, L., Shi, Y., and Duffy, C.: Understanding watershed hydrogeochemistry: 1. Development of RT -  
777 Flux - PIHM, *Water Resources Research*, 53, 2328-2345, 2017.
- 778 Basu, N. B., Destouni, G., Jawitz, J. W., Thompson, S. E., Loukinova, N. V., Darracq, A., Zanardo, S., Yaeger,  
779 M., Sivapalan, M., Rinaldo, A., and Rao, P. S. C.: Nutrient loads exported from managed catchments reveal  
780 emergent biogeochemical stationarity, *Geophys. Res. Lett.*, 37, 10.1029/2010GL045168, 2010.
- 781 Benettin, P., Fovet, O., and Li, L.: Nitrate removal and young stream water fractions at the catchment  
782 scale, *Hydrological Processes*, 34, 2725-2738, <https://doi.org/10.1002/hyp.13781>, 2020.
- 783 Beven, K.: How far can we go in distributed hydrological modelling?, *Hydrol. Earth Syst. Sci.*, 5, 1-12,  
784 10.5194/hess-5-1-2001, 2001.
- 785 Beven, K.: A manifesto for the equifinality thesis, *Journal of Hydrology*, 320, 18-36,  
786 10.1016/j.jhydrol.2005.07.007, 2006.
- 787 Beven, K., and Lane, S.: Invalidation of Models and Fitness-for-Purpose: A Rejectionist Approach, in:  
788 *Computer Simulation Validation: Fundamental Concepts, Methodological Frameworks, and Philosophical*  
789 *Perspectives*, edited by: Beisbart, C., and Saam, N. J., Springer International Publishing, Cham, 145-171,  
790 2019.
- 791 Bhatt, G., Kumar, M., and Duffy, C. J.: A tightly coupled GIS and distributed hydrologic modeling  
792 framework, *Environmental Modelling & Software*, 62, 70-84,  
793 <http://dx.doi.org/10.1016/j.envsoft.2014.08.003>, 2014.
- 794 Botter, M., Li, L., Hartmann, J., Burlando, P., and Fatichi, S.: Depth of Solute Generation Is a Dominant  
795 Control on Concentration-Discharge Relations, *Water Resources Research*, 56, e2019WR026695,  
796 <https://doi.org/10.1029/2019WR026695>, 2020.
- 797 Bracho, R., Natali, S., Pegoraro, E., Crummer, K. G., Schädel, C., Celis, G., Hale, L., Wu, L., Yin, H., and Tiedje,  
798 J. M.: Temperature sensitivity of organic matter decomposition of permafrost-region soils during  
799 laboratory incubations, *Soil Biology and Biochemistry*, 97, 1-14, 2016.
- 800 Brantley, S. L., Kubicki, J. D., and White, A. F.: Kinetics of water-rock interaction, 2008.
- 801 Brantley, S. L., White, T., West, N., Williams, J. Z., Forsythe, B., Shapich, D., Kaye, J., Lin, H., Shi, Y. N., Kaye,  
802 M., Herndon, E., Davis, K. J., He, Y., Eissenstat, D., Weitzman, J., DiBiase, R., Li, L., Reed, W., Brubaker, K.,  
803 and Gu, X.: Susquehanna Shale Hills Critical Zone Observatory: Shale Hills in the Context of Shaver's Creek  
804 Watershed, *Vadose Zone Journal*, 17, 1-19, ARTN 180092  
805 10.2136/vzj2018.04.0092, 2018.
- 806 Buljovic, Z., and Engels, C.: Nitrate uptake ability by maize roots during and after drought stress, *Plant*  
807 *and Soil*, 229, 125-135, 2001.



808 Buysse, J., Smolders, E., and Merckx, R.: Modelling the uptake of nitrate by a growing plant with an  
809 adjustable root nitrate uptake capacity, *Plant and Soil*, 181, 19-23, 1996.

810 Cai, X., Yang, Z.-L., Fisher, J., Zhang, X., Barlage, M., and Chen, F.: Integration of nitrogen dynamics into  
811 the Noah-MP land surface model v1. 1 for climate and environmental predictions, *Geoscientific Model  
812 Development (Online)*, 9, 2016.

813 Davidson, E. A., and Janssens, I. A.: Temperature sensitivity of soil carbon decomposition and feedbacks  
814 to climate change, *Nature*, 440, 165-173, 10.1038/nature04514, 2006.

815 Davidson, E. A., Janssens, I. A., and Luo, Y.: On the variability of respiration in terrestrial ecosystems:  
816 moving beyond Q10, *Global Change Biology*, 12, 154-164, 2006.

817 Davidson, E. A., Janssens, I.A.: Temperature sensitivity of soil carbon decomposition and feedbacks to  
818 climate change, *Nature*, 440, 165-173, 2006.

819 Di Capua, F., Pirozzi, F., Lens, P. N. L., and Esposito, G.: Electron donors for autotrophic denitrification,  
820 *Chemical Engineering Journal*, 362, 922-937, <https://doi.org/10.1016/j.cej.2019.01.069>, 2019.

821 Dingman, S. L.: *Physical hydrology*, Waveland press, 2015.

822 Dunbabin, V. M., Diggle, A. J., Rengel, Z., and Van Hugten, R.: Modelling the interactions between water  
823 and nutrient uptake and root growth, *Plant and Soil*, 239, 19-38, 2002.

824 Fatichi, S., Vivoni, E. R., Ogden, F. L., Ivanov, V. Y., Mirus, B., Gochis, D., Downer, C. W., Camporese, M.,  
825 Davison, J. H., and Ebel, B.: An overview of current applications, challenges, and future trends in  
826 distributed process-based models in hydrology, *Journal of Hydrology*, 537, 45-60, 2016.

827 Fatichi, S., Manzoni, S., Or, D., and Paschalis, A.: A Mechanistic Model of Microbially Mediated Soil  
828 Biogeochemical Processes: A Reality Check, *Global Biogeochemical Cycles*, 33, 620-648,  
829 10.1029/2018gb006077, 2019.

830 Fisher, J., Sitch, S., Malhi, Y., Fisher, R., Huntingford, C., and Tan, S. Y.: Carbon cost of plant nitrogen  
831 acquisition: A mechanistic, globally applicable model of plant nitrogen uptake, retranslocation, and  
832 fixation, *Global Biogeochemical Cycles*, 24, 2010.

833 Friedlingstein, P., Cox, P., Betts, R., Bopp, L., von Bloh, W., Brovkin, V., Cadule, P., Doney, S., Eby, M., and  
834 Fung, I.: Climate-carbon cycle feedback analysis: results from the C4MIP model intercomparison, *Journal  
835 of climate*, 19, 3337-3353, 2006.

836 Gatel, L., Lauvernet, C., Carluer, N., Weill, S., Tournebize, J., and Paniconi, C.: Global evaluation and  
837 sensitivity analysis of a physically based flow and reactive transport model on a laboratory experiment,  
838 *Environmental Modelling & Software*, 113, 73-83, <https://doi.org/10.1016/j.envsoft.2018.12.006>, 2019.

839 Godsey, S. E., Kirchner, J. W., and Clow, D. W.: Concentration-discharge relationships reflect chemostatic  
840 characteristics of US catchments, *Hydrol. Process.*, 23, 1844-1864, 10.1002/hyp.7315, 2009.

841 Godsey, S. E., Hartmann, J., and Kirchner, J. W.: Catchment chemostasis revisited: Water quality responds  
842 differently to variations in weather and climate, *Hydrological Processes*, 33, 3056-3069,  
843 <https://doi.org/10.1002/hyp.13554>, 2019.

844 Grathwohl, P., Rügner, H., Wöhling, T., Osenbrück, K., Schwientek, M., Gayler, S., Wollschläger, U., Selle,  
845 B., Pause, M., and Delfs, J.-O.: Catchments as reactors: a comprehensive approach for water fluxes and  
846 solute turnover, *Environmental earth sciences*, 69, 317-333, 2013.

847 Green, T. R.: Linking climate change and groundwater, in: *Integrated groundwater management*, Springer,  
848 Cham, 97-141, 2016.

849 Gurdak, J. J.: Groundwater: Climate-induced pumping, *Nature Geoscience*, 10, 71, 2017.

850 Hamamoto, S., Moldrup, P., Kawamoto, K., and Komatsu, T.: Excluded - volume expansion of Archie's law  
851 for gas and solute diffusivities and electrical and thermal conductivities in variably saturated porous  
852 media, *Water Resources Research*, 46, 2010.

853 Han, B., Benner, S. G., and Flores, A. N.: Including Variability across Climate Change Projections in  
854 Assessing Impacts on Water Resources in an Intensively Managed Landscape, *Water*, 11, 286, 2019.

855 Hararuk, O., Smith, M. J., and Luo, Y.: Microbial models with data-driven parameters predict stronger soil  
856 carbon responses to climate change, *Glob. Chang. Biol.*, 21, 2439-2453, 10.1111/gcb.12827, 2015.

857 HARTLEY, I. P., HEINEMEYER, A., and INESON, P.: Effects of three years of soil warming and shading on the  
858 rate of soil respiration: substrate availability and not thermal acclimation mediates observed response,  
859 *Global Change Biology*, 13, 1761-1770, <https://doi.org/10.1111/j.1365-2486.2007.01373.x>, 2007.

860 Hartmann, J., Lauerwald, R., and Moosdorf, N.: A brief overview of the GLObal River CHEmistry Database,  
861 *GLORICH, Procedia Earth and Planetary Science*, 10, 23-27, 2014.

862 Hasenmueller, E. A., Jin, L., Stinchcomb, G. E., Lin, H., Brantley, S. L., and Kaye, J. P.: Topographic controls  
863 on the depth distribution of soil CO<sub>2</sub> in a small temperate watershed, *Applied Geochemistry*, 63, 58-69,  
864 2015.

865 Hasenmueller, E. A., Gu, X., Weitzman, J. N., Adams, T. S., Stinchcomb, G. E., Eissenstat, D. M., Drohan, P.  
866 J., Brantley, S. L., and Kaye, J. P.: Weathering of rock to regolith: The activity of deep roots in bedrock  
867 fractures, *Geoderma*, 300, 11-31, 2017.

868 Heidari, P., Li, L., Jin, L., Williams, J. Z., and Brantley, S. L.: A reactive transport model for Marcellus shale  
869 weathering, *Geochimica et Cosmochimica Acta*, 217, 421-440, 2017.

870 Herndon, E. M., Dere, A. L., Sullivan, P. L., Norris, D., Reynolds, B., and Brantley, S. L.: Landscape  
871 heterogeneity drives contrasting concentration–discharge relationships in shale headwater catchments,  
872 *Hydrology and earth system sciences*, 19, 3333-3347, 2015.

873 Hindmarsh, A. C., Brown, P. N., Grant, K. E., Lee, S. L., Serban, R., Shumaker, D. E., and Woodward, C. S.:  
874 SUNDIALS: Suite of nonlinear and differential/algebraic equation solvers, *ACM Transactions on*  
875 *Mathematical Software (TOMS)*, 31, 363-396, 2005.

876 Hubbard, S. S., Williams, K. H., Agarwal, D., Banfield, J., Beller, H., Bouskill, N., Brodie, E., Carroll, R.,  
877 Dafflon, B., and Dwivedi, D.: The East River, Colorado, Watershed: A mountainous community testbed for  
878 improving predictive understanding of multiscale hydrological–biogeochemical dynamics, *Vadose Zone*  
879 *Journal*, 17, 2018.

880 Husic, A.: Numerical modeling and isotope tracers to investigate karst biogeochemistry and transport  
881 processes, 2018.

882 Jin, L., and Brantley, S. L.: Soil chemistry and shale weathering on a hillslope influenced by convergent  
883 hydrologic flow regime at the Susquehanna/Shale Hills Critical Zone Observatory, *Applied Geochemistry*,  
884 26, Supplement, S51-S56, <http://dx.doi.org/10.1016/j.apgeochem.2011.03.027>, 2011.

885 Jin, L. X., Ravella, R., Ketchum, B., Bierman, P. R., Heaney, P., White, T., and Brantley, S. L.: Mineral  
886 weathering and elemental transport during hillslope evolution at the Susquehanna/Shale Hills Critical  
887 Zone Observatory, *Geochim Cosmochim Acta*, 74, 3669-3691, 10.1016/j.gca.2010.03.036, 2010.

888 Keune, J., Gasper, F., Goergen, K., Hense, A., Shrestha, P., Sulis, M., and Kollet, S.: Studying the influence  
889 of groundwater representations on land surface-atmosphere feedbacks during the European heat wave  
890 in 2003, *Journal of Geophysical Research: Atmospheres*, 121, 13,301-313,325,  
891 <https://doi.org/10.1002/2016JD025426>, 2016.

892 Kirchner, J. W., Hooper, R. P., Kendall, C., Neal, C., and Leavesley, G.: Testing and validating environmental  
893 models, *Science of the Total Environment*, 183, 33-47, 10.1016/0048-9697(95)04971-1, 1996.

894 Kuntz, B. W., Rubin, S., Berkowitz, B., and Singha, K.: Quantifying Solute Transport at the Shale Hills Critical  
895 Zone Observatory, *Vadose Zone Journal*, 10, 843-857, 10.2136/vzj2010.0130, 2011.

896 Leonard, L., and Duffy, C. J.: Essential terrestrial variable data workflows for distributed water resources  
897 modeling, *Environmental modelling & software*, 50, 85-96, 2013.

898 Li, L., Salehikhoo, F., Brantley, S. L., and Heidari, P.: Spatial zonation limits magnesite dissolution in porous  
899 media, *Geochimica et Cosmochimica Acta*, 126, 555-573, 10.1016/j.gca.2013.10.051, 2014.

900 Li, L., Bao, C., Sullivan, P. L., Brantley, S., Shi, Y., and Duffy, C.: Understanding watershed  
901 hydrogeochemistry: 2. Synchronized hydrological and geochemical processes drive stream chemostatic  
902 behavior, *Water Resources Research*, 53, 2346-2367, 2017a.

903 Li, L., Maher, K., Navarre-Sitchler, A., Druhan, J., Meile, C., Lawrence, C., Moore, J., Perdrial, J., Sullivan, P.,  
904 Thompson, A., Jin, L., Bolton, E. W., Brantley, S. L., Dietrich, W. E., Mayer, K. U., Steefel, C. I., Valocchi, A.,  
905 Zachara, J., Kocar, B., McIntosh, J., Tutolo, B. M., Kumar, M., Sonnenthal, E., Bao, C., and Beisman, J.:  
906 Expanding the role of reactive transport models in critical zone processes, *Earth-Science Reviews*, 165,  
907 280-301, <http://dx.doi.org/10.1016/j.earscirev.2016.09.001>, 2017b.

908 Li, L.: Watershed reactive transport, *Reviews in Mineralogy and Geochemistry*, 85, 381-418, 2019.

909 Li, L., Sullivan, P. L., Benettin, P., Cirpka, O. A., Bishop, K., Brantley, S. L., Knapp, J. L. A., Meerveld, I.,  
910 Rinaldo, A., Seibert, J., Wen, H., and Kirchner, J. W.: Toward catchment hydro - biogeochemical theories,  
911 *WIREs Water*, 10.1002/wat2.1495, 2020.

912 Lin, H.: Temporal stability of soil moisture spatial pattern and subsurface preferential flow pathways in  
913 the Shale Hills Catchment, *Vadose Zone Journal*, 5, 317-340, 2006.

914 Lindström, G., Rosberg, J., and Arheimer, B.: Parameter Precision in the HBV-NP Model and Impacts on  
915 Nitrogen Scenario Simulations in the Rönneå River, Southern Sweden, *AMBIO: A Journal of the Human  
916 Environment*, 34, 533-537, 535, 2005.

917 Lindström, G., Pers, C., Rosberg, J., Strömqvist, J., and Arheimer, B.: Development and testing of the HYPE  
918 (Hydrological Predictions for the Environment) water quality model for different spatial scales, *Hydrology  
919 Research*, 41, 295-319, 10.2166/nh.2010.007, 2010.

920 Liu, Y., Wang, C., He, N., Wen, X., Gao, Y., Li, S., Niu, S., Butterbach - Bahl, K., Luo, Y., and Yu, G.: A global  
921 synthesis of the rate and temperature sensitivity of soil nitrogen mineralization: latitudinal patterns and  
922 mechanisms, *Global change biology*, 23, 455-464, 2017.

923 Lloyd, J., and Taylor, J. A.: On the Temperature Dependence of Soil Respiration, *Functional Ecology*, 8, 315-  
924 323, 10.2307/2389824, 1994.

925 López, B., Sabaté, S., and Gracia, C.: Vertical distribution of fine root density, length density, area index  
926 and mean diameter in a *Quercus ilex* forest, *Tree Physiology*, 21, 555-560, 2001.

927 McMurtrie, R. E., Iversen, C. M., Dewar, R. C., Medlyn, B. E., Näsholm, T., Pepper, D. A., and Norby, R. J.:  
928 Plant root distributions and nitrogen uptake predicted by a hypothesis of optimal root foraging, *Ecology  
929 and Evolution*, 2, 1235-1250, 2012.

930 Miller, M. P., Tesoriero, A. J., Hood, K., Terziotti, S., and Wolock, D. M.: Estimating Discharge and Nonpoint  
931 Source Nitrate Loading to Streams From Three End-Member Pathways Using High-Frequency Water  
932 Quality Data, *Water Resources Research*, 53, 10201-10216, 10.1002/2017wr021654, 2017.

933 Miller, M. P., Capel, P. D., García, A. M., and Ator, S. W.: Response of Nitrogen Loading to the Chesapeake  
934 Bay to Source Reduction and Land Use Change Scenarios: A SPARROW - Informed Analysis, *JAWRA  
935 Journal of the American Water Resources Association*, 56, 100-112, 2020.

936 Moatar, F., Abbott, B. W., Minaudo, C., Curie, F., and Pinay, G.: Elemental properties, hydrology, and  
937 biology interact to shape concentration - discharge curves for carbon, nutrients, sediment, and major  
938 ions, *Water Resources Research*, 53, 1270-1287, 2017.

939 Moriasi, D. N., Arnold, J. G., Van Liew, M. W., Bingner, R. L., Harmel, R. D., and Veith, T. L.: Model evaluation  
940 guidelines for systematic quantification of accuracy in watershed simulations, *T Asabe*, 50, 885-900, 2007.

941 Moriasi, D. N., Gitau, M. W., Pai, N., and Daggupati, P.: Hydrologic and water quality models: Performance  
942 measures and evaluation criteria, *T Asabe*, 58, 1763-1785, 2015.

943 Musolff, A., Schmidt, C., Selle, B., and Fleckenstein, J. H.: Catchment controls on solute export, *Adv. Water  
944 Resour.*, 86, 133-146, 10.1016/j.advwatres.2015.09.026, 2015.

945 Neitsch, S. L., Arnold, J. G., Kiniry, J. R., and Williams, J. R.: Soil and water assessment tool theoretical  
946 documentation version 2009, Texas Water Resources Institute, 2011.

947 Porporato, A., D'odorico, P., Laio, F., and Rodriguez-Iturbe, I.: Hydrologic controls on soil carbon and  
948 nitrogen cycles. I. Modeling scheme, *Advances in water resources*, 26, 45-58, 2003.

949 Qu, Y., and Duffy, C. J.: A semidiscrete finite volume formulation for multiprocess watershed simulation,  
950 *Water Resources Research*, 43, W08419, 2007.

951 Regnier, P., and Steefel, C. I.: A high resolution estimate of the inorganic nitrogen flux from the Scheldt  
952 estuary to the coastal North Sea during a nitrogen-limited algal bloom, spring 1995, *Geochimica et*  
953 *Cosmochimica Acta*, 63, 1359-1374, 10.1016/s0016-7037(99)00034-4, 1999.

954 Rutherford, D. W., Chiou, C. T., and Kile, D. E.: Influence of soil organic matter composition on the partition  
955 of organic compounds, *Environmental science & technology*, 26, 336-340, 1992.

956 Saad, Y., and Schultz, M. H.: GMRES: A generalized minimal residual algorithm for solving nonsymmetric  
957 linear systems, *SIAM Journal on scientific and statistical computing*, 7, 856-869, 1986.

958 Saberi, L., Crystal Ng, G. H., Nelson, L., Zhi, W., Li, L., La Frenierre, J., and Johnstone, M.: Spatiotemporal  
959 Drivers of Hydrochemical Variability in a Tropical Glacierized Watershed in the Andes, *Water Resources*  
960 *Research*, 57, e2020WR028722, 2021.

961 Scudeler, C., Pangle, L., Pasetto, D., Niu, G.-Y., Volkmann, T., Paniconi, C., Putti, M., and Troch, P.:  
962 Multiresponse modeling of variably saturated flow and isotope tracer transport for a hillslope experiment  
963 at the Landscape Evolution Observatory, *Hydrology and Earth System Sciences*, 20, 4061-4078, 2016.

964 Sebestyen, S. D., Ross, D. S., Shanley, J. B., Elliott, E. M., Kendall, C., Campbell, J. L., Dail, D. B., Fernandez,  
965 I. J., Goodale, C. L., and Lawrence, G. B.: Unprocessed Atmospheric Nitrate in Waters of the Northern  
966 Forest Region in the US and Canada, *Environmental science & technology*, 53, 3620-3633, 2019.

967 Seibert, J., Grabs, T., Köhler, S., Laudon, H., Winterdahl, M., and Bishop, K.: Linking soil- and stream-water  
968 chemistry based on a Riparian Flow-Concentration Integration Model, *Hydrol. Earth Syst. Sci.*, 13, 2287-  
969 2297, 10.5194/hess-13-2287-2009, 2009.

970 Shi, Y.: Development of a land surface hydrologic modeling and data assimilation system for the study of  
971 subsurface-land surface interaction, 2012.

972 Shi, Y., Davis, K. J., Duffy, C. J., and Yu, X.: Development of a coupled land surface hydrologic model and  
973 evaluation at a critical zone observatory, *Journal of Hydrometeorology*, 14, 1401-1420, 2013.

974 Skamarock, W., and Klemp, J.: A Description of the Advanced Research WRF Model Version 4. Ncar  
975 Technical Notes, No, NCAR/TN-556+ STR, 2019.

976 Steefel, C., Appelo, C., Arora, B., Jacques, D., Kalbacher, T., Kolditz, O., Lagneau, V., Lichtner, P., Mayer, K.  
977 U., and Meeussen, J.: Reactive transport codes for subsurface environmental simulation, *Computational*  
978 *Geosciences*, 19, 445-478, 2015.

979 Steefel, C. I., and Lasaga, A. C.: A coupled model for transport of multiple chemical species and kinetic  
980 precipitation/dissolution reactions with application to reactive flow in single phase hydrothermal systems,  
981 *American Journal of science*, 294, 529-592, 1994.

982 Sullivan, P. L., Hynek, S. A., Gu, X., Singha, K., White, T., West, N., Kim, H., Clarke, B., Kirby, E., Duffy, C.,  
983 and Brantley, S. L.: Oxidative dissolution under the channel leads geomorphological evolution at the Shale  
984 Hills catchment, *American Journal of Science*, 316, 981-1026, 10.2475/10.2016.02, 2016.

985 Taylor, R. G., Scanlon, B., Döll, P., Rodell, M., Van Beek, R., Wada, Y., Longuevergne, L., Leblanc, M.,  
986 Famiglietti, J. S., and Edmunds, M.: Ground water and climate change, *Nature climate change*, 3, 322,  
987 2013.

988 van der Velde, Y., de Rooij, G. H., Rozemeijer, J. C., van Geer, F. C., and Broers, H. P.: Nitrate response of  
989 a lowland catchment: On the relation between stream concentration and travel time distribution  
990 dynamics, *Water Resources Research*, 46, 10.1029/2010wr009105, 2010.

991 van der Velde, Y., Vercauteren, N., Jaramillo, F., Dekker, S. C., Destouni, G., and Lyon, S. W.: Exploring  
992 hydroclimatic change disparity via the Budyko framework, *Hydrological Processes*, 28, 4110-4118,  
993 10.1002/hyp.9949, 2014.

994 Weiler, M., and McDonnell, J. R. J.: Testing nutrient flushing hypotheses at the hillslope scale: A virtual  
995 experiment approach, *J. Hydrol.*, 319, 339-356, 10.1016/j.jhydrol.2005.06.040, 2006.

996 Weitzman, J. N., and Kaye, J. P.: Nitrogen Budget and Topographic Controls on Nitrous Oxide in a Shale -  
997 Based Watershed, *Journal of Geophysical Research: Biogeosciences*, 123, 1888-1908, 2018.

998 Wen, H., and Li, L.: An upscaled rate law for magnesite dissolution in heterogeneous porous media,  
999 *Geochimica et Cosmochimica Acta*, 210, 289-305, 2017.

1000 Wen, H., and Li, L.: An upscaled rate law for mineral dissolution in heterogeneous media: The role of time  
1001 and length scales, *Geochimica et Cosmochimica Acta*, 235, 1-20, 2018.

1002 Wen, H., Perdrial, J., Bernal, S., Abbott, B. W., Dupas, R., Godsey, S. E., Harpold, A., Rizzo, D., Underwood,  
1003 K., and Adler, T.: Temperature controls production but hydrology controls export of dissolved organic  
1004 carbon at the catchment scale, 24, 945-966, 2020.

1005 Wen, H., Brantley, S. L., Davis, K. J., Duncan, J. M., and Li, L.: The Limits of Homogenization: What  
1006 Hydrological Dynamics can a Simple Model Represent at the Catchment Scale?, *Water Resources*  
1007 *Research*, 57, e2020WR029528, <https://doi.org/10.1029/2020WR029528>, 2021.

1008 Wolery, T. J.: EQ3/6, a software package for geochemical modeling of aqueous systems: package overview  
1009 and installation guide (version 7.0), 1992.

1010 Xiao, D., Shi, Y., Brantley, S. L., Forsythe, B., DiBiase, R., Davis, K., and Li, L.: Streamflow Generation From  
1011 Catchments of Contrasting Lithologies: The Role of Soil Properties, Topography, and Catchment Size,  
1012 *Water Resources Research*, n/a, 10.1029/2018wr023736, 2019.

1013 Xiao, D., Brantley, S. L., and Li, L.: Vertical Connectivity Regulates Water Transit Time and Chemical  
1014 Weathering at the Hillslope Scale, *Water Resources Research*, 57, e2020WR029207,  
1015 <https://doi.org/10.1029/2020WR029207>, 2021.

1016 Yan, Q., Duan, Z., Mao, J., Li, X., and Dong, F.: Effects of root-zone temperature and N, P, and K supplies  
1017 on nutrient uptake of cucumber (*Cucumis sativus* L.) seedlings in hydroponics, *Soil Science and Plant*  
1018 *Nutrition*, 58, 707-717, 2012.

1019 Yan, Z., Bond-Lamberty, B., Todd-Brown, K. E., Bailey, V. L., Li, S., Liu, C., and Liu, C.: A moisture function  
1020 of soil heterotrophic respiration that incorporates microscale processes, *Nat Commun*, 9, 2562,  
1021 10.1038/s41467-018-04971-6, 2018.

1022 Zarnetske, J. P., Bouda, M., Abbott, B. W., Saiers, J., and Raymond, P. A.: Generality of hydrologic transport  
1023 limitation of watershed organic carbon flux across ecoregions of the United States, *Geophysical Research*  
1024 *Letters*, 45, 11,702-711,711, 2018.

1025 Zhi, W., Li, L., Dong, W., Brown, W., Kaye, J., Steefel, C., and Williams, K. H.: Distinct Source Water  
1026 Chemistry Shapes Contrasting Concentration-Discharge Patterns, *Water Resour. Res.*, 55, 4233-4251,  
1027 10.1029/2018wr024257, 2019.

1028 Zhi, W., and Li, L.: The Shallow and Deep Hypothesis: Subsurface Vertical Chemical Contrasts Shape Nitrate  
1029 Export Patterns from Different Land Uses, *Environmental Science & Technology*, 54, 11915-11928,  
1030 10.1021/acs.est.0c01340, 2020.

1031 Zhou, T., Shi, P., Hui, D., and Luo, Y.: Global pattern of temperature sensitivity of soil heterotrophic  
1032 respiration (Q10) and its implications for carbon - climate feedback, *Journal of Geophysical Research:*  
1033 *Biogeosciences*, 114, 2009.

1034